



Heatline analysis on natural convection for nanofluids confined within square cavities with various thermal boundary conditions

Tanmay Basak^a, Ali J. Chamkha^{b,*}

^a Department of Chemical Engineering, Indian Institute of Technology Madras, Chennai 600036, India

^b Manufacturing Engineering Department, The Public Authority for Applied Education and Training, Shuweikh 70654, Kuwait

ARTICLE INFO

Article history:

Received 8 October 2011

Received in revised form 4 May 2012

Accepted 12 May 2012

Available online 25 June 2012

Keywords:

Heatlines

Heatfunctions

Nanofluid

Natural convection

Square cavity

Uniform and non-uniform heating

ABSTRACT

Natural convection of nanofluids in presence of hot and cold side walls (case 1) or uniform or non-uniform heating of bottom wall with cold side walls (case 2) have been investigated based on visualization of heat flow via heatfunctions or heatlines. Galerkin finite element method has been employed to solve momentum and energy balance as well as post processing streamfunctions and heatfunctions. Various nanofluids are considered as Copper–Water, TiO₂–Water and Alumina–Water. Enhancement of heat transfer with respect to base fluid (water) has been observed for all ranges of Rayleigh number (Ra). Dominance of viscous force or buoyancy force are found to play significant roles to characterize the heat transfer rates and temperature patterns which are also established based on heatlines. In general, convective closed loop heatlines are present even at low Rayleigh number ($Ra = 10^3$) within base fluid, but all nanofluids exhibit dominant conductive heat transport as the flow is also found to be weak due to dominance of viscous force for case 1. On the other hand, convective heat transport at the core of a circulation cell, typically represented by closed loop heatlines, is more intense for nanofluids compared to base fluid (water) for case 2 at $Ra = 10^5$. It is also found that heatlines with larger heatfunction values for nanofluids coincide with heatlines with smaller heatfunction values for water at walls. Consequently, Nusselt number which is also correlated with heatfunctions show larger values of nanofluids for all ranges of Ra . Average Nusselt numbers show that larger enhancement of heat transfer rates for all nanofluids at $Ra = 10^5$ and Alumina–Water and Copper–Water exhibit larger enhancement of heat transfer rates.

© 2012 Elsevier Ltd. All rights reserved.

1. Introduction

A nanofluid is a base fluid with suspended metallic nanoparticles [1]. As traditional fluids used for heat transfer applications such as water, mineral oils and ethylene glycol have a rather low thermal conductivity, nanofluids with relatively higher thermal conductivities have attracted enormous interest from researchers due to their potential in enhancement of heat transfer with little or no penalty in pressure drop. Eastman et al. [2] showed that an increase in thermal conductivity of approximately 60% can be obtained for a nanofluid consisting of water and 5 volume % CuO nanoparticles. This is attributed to the increase in surface area due to the suspension of nanoparticles. Also, it was reported that a small amount (less than 1% volume fraction) of copper nanoparticles or carbon nanotubes dispersed in ethylene glycol or oil can increase their inherently poor thermal conductivity by 40% and 150%, respectively [3,4]. Das et al. [5] reported a 24-fold increase

in thermal conductivity enhancement for water-based nanofluids containing Al₂O₃ or CuO nanoparticles over a small temperature range, 21–51 °C. Koblinski et al. [6] reported on the possible mechanisms of enhancing thermal conductivity, and suggested that the size effect, the clustering of nanoparticles and the surface adsorption could be the major reason of enhancement, while the Brownian motion of nanoparticles contributes much less than other factors since Brownian motion of nanoparticles is too slow to transport significant amount of heat through a nanofluid and this conclusion was also supported by their results of molecular dynamics simulation. Wang et al. [7] have studied experimentally the effective thermal conductivity of liquids with 25 nm SiO₂ particle inclusions and observed the percolation pattern of particle clustering by scanning tunnel microscopic (STM) photos. It was believed that clustering could affect the enhancement prominently. Wang et al. [8] have used a fractal model for predicting the effective thermal conductivity of liquid with suspension of nano-particles and found that it predicts well the trend for variation of the effective thermal conductivity with dilute suspension of nanoparticles. Several other models have been proposed for calculating the effective apparent thermal conductivity of a solid–fluid system [9–13].

* Corresponding author.

E-mail addresses: tanmay@iitm.ac.in (T. Basak), achamkha@yahoo.com (A.J. Chamkha).

Nomenclature

| | |
|-------|---|
| C_p | specific heat, $\text{J kg}^{-1} \text{K}^{-1}$ |
| g | acceleration due to gravity, m s^{-2} |
| k | thermal conductivity, $\text{W m}^{-1} \text{K}^{-1}$ |
| L | side of the square cavity, m |
| N | total number of nodes |
| p | pressure, Pa |
| P | dimensionless pressure |
| Pr | Prandtl number |
| R | residual of weak form |
| Ra | Rayleigh number |
| T | temperature, K |
| T_h | temperature of hot bottom wall, K |
| T_c | temperature of cold vertical wall, K |
| u | x component of velocity |
| U | x component of dimensionless velocity |
| v | y component of velocity |
| V | y component of dimensionless velocity |
| X | dimensionless distance along x coordinate |
| x | distance along x coordinate |
| Y | dimensionless distance along y coordinate |

| | |
|-----|-------------------------------|
| y | distance along y coordinate |
|-----|-------------------------------|

Greek symbols

| | |
|----------|---|
| α | thermal diffusivity, $\text{m}^2 \text{s}^{-1}$ |
| β | volume expansion coefficient, K^{-1} |
| γ | penalty parameter |
| Γ | boundary |
| θ | dimensionless temperature |
| ν | kinematic viscosity, $\text{m}^2 \text{s}^{-1}$ |
| ρ | density, kg m^{-3} |
| Φ | basis functions |
| ψ | streamfunction |
| Π | heatfunction |

Subscripts

| | |
|------|-----------------|
| i | residual number |
| k | node number |
| f | base fluid |
| nf | nanofluid |
| p | solid particles |

The convective heat transfer characteristic of nanofluids depends on the thermo-physical properties of the base fluid and the ultra fine particles, the flow pattern and flow structure, the volume fraction of the suspended particles, the dimensions and the shape of these particles. The utility of a particular nanofluid for a heat transfer application can be established by suitably modeling the convective transport in the nanofluid [14]. Several studies of convective heat transfer in nanofluids have been reported in recent years. Khanafer et al. [15] investigated the problem of buoyancy-driven heat transfer enhancement of nanofluids in a two-dimensional enclosure. A few earlier works [16–21] involve studies on free convection in rectangular enclosures with nanofluids and enhancement of heat transfer rate was found. Santra et al. [22] conducted a study of heat transfer augmentation in a differentially heated square cavity using Copper–Water nanofluid using the models proposed by Maxwell–Garnett [11] and Bruggeman [12]. Ho et al. [23] reported a numerical simulation of natural convection of nanofluid in a square enclosure considering the effects due to uncertainties of viscosity and thermal conductivity. Oztop and Abu-Nada [24] studied heat transfer and fluid flow due to buoyancy forces in a partially heated enclosure using nanofluids with various types of nanoparticles and found heat transfer enhancement at a low aspect ratio. Abu-Nada [25] reported on the application of nanofluids for heat transfer enhancement of separated flows encountered in a backward facing step. Further, the effects of variable viscosity and thermal conductivity of Al_2O_3 –Water nanofluid on heat transfer enhancement in natural convection were studied [26]. Enhancement of heat transfer with nanofluids was also found to occur in various applications such as natural convection cooling of a localized heat source [27], natural convection in enclosures with various inclinations [28], periodic natural convection in a nanofluid-filled enclosure with oscillating heat flux [29], natural convection in enclosures with one side is sinusoidally heated or cooled [30], natural convection in an inclined enclosure with a heat source [31], experimental studies on natural convection in vertical square enclosures [32], natural convection within a cavity with two pairs of heat source-sink [33], etc. Nield and Kuznetsov [34] carried out analytical investigations on the effect of vertical throughflow on the onset of convection in a horizontal layer of porous medium saturated with nanofluid. Their study primarily focuses on the dependence of the critical Rayleigh number for the non-oscillatory and oscillatory modes of instability on the

thermophoresis and Brownian motion parameters for the cases with and without throughflow. Arifin et al. [35] investigated a non-isobaric Marangoni boundary layer flow that can be formed along the interface of immiscible nanofluids in surface driven flows due to an imposed temperature gradient. They found dual solutions for specific parameters. Ghasemi et al. [36] investigated the natural convection in an enclosure that is filled with a water– Al_2O_3 nanofluid and is influenced by a magnetic field. Their results show that the heat transfer rate increases with Rayleigh number, but that decreases with an increase of the Hartmann number.

Although significant amount of works were carried out for the role of nanofluid on enhancement of heat transfer, but the detailed visualization on heat transport is yet to appear in the literature. The studies on visualization of heat transfer is important and that may further add new insight to assess the role of nanofluid on the local and overall heat transfer enhancements. In general, the visualization of heat transfer is carried out using heatlines. Till date, heatline based analysis on the evaluation of heat transfer enhancement for natural convection in nanofluids within enclosures is yet to appear in literature.

Heatline concept was developed by earlier researchers [37,38] to visualize conductive as well as convective heat transport. Heatlines typically represent heatfunctions which are energy analog of streamfunctions in such a way that the former intrinsically satisfies the thermal energy equation for energy flows while the later plays the same role in mass continuity equation to explain fluid dynamics. Heatlines are mathematically represented by heatfunctions which are in turn related to Nusselt number based on proper dimensionless form.

A few earlier researchers analyzed heatline concept for various physical situations [39–49]. Bello-Ochende [39] studied Poisson-type heatfunction for thermal convection in a square cavity. Morega and Bejan [40] extended the heatline visualization tool to the most basic and simplest form of convective heat transfer through the laminar boundary layer on flat plate with uniform temperature or flux. Zhao et al. [41] studied the application issues in streamlines, heatlines and masslines for conjugate heat and mass transfer using numerical viewpoints and established that heatlines and masslines are useful tools to discuss the convective heat and mass transfer. They reported that visualization results by streamlines, heatlines and masslines directly exhibit the nature of the fluid, heat and mass transports through each cavity and also

through the diffusive walls and solid bodies. Costa [42] implemented a unified approach to visualize the two dimensional transport phenomena and presented a general physical and numerical treatment for functions and lines used for visualization. Review on Bejan's heatlines and masslines for convection visualization was also presented by Costa [43]. Dash [44] introduced the concept of a heatfunction to visualize the path of heat flow in a buoyancy-driven turbulent flow using heated vertical flat plate. Zhao et al. [45] carried out numerical studies with streamlines, heatlines and masslines of steady state double-diffusive natural convection induced by bottom heating and polluting with two finite thermal and pollutant strips. A few other applications on heatlines studies involve forced convection in a porous media [46], double-diffusive convection in a porous enclosure [47] and conjugate natural convection/heat conduction [48,49].

The objective of this article is to analyze the flow and thermal characteristics of water and nanofluids (Cu–Water, TiO₂–Water and Alumina–Water) confined within square cavity with various heating patterns of walls. Numerical investigations on heating characteristics within square cavities have been carried out based on coupled partial differential equations of momentum and energy which are solved using Galerkin finite element method with penalty parameter to obtain the numerical simulations in terms of streamfunctions, heatfunctions and isotherms. The streamfunctions and heatfunctions of Poisson equation are also solved using Galerkin finite element method. The jump discontinuity in Dirichlet type of wall boundary conditions for temperature at the corner points is tackled by implementation of exact boundary conditions at those singular points as mentioned earlier [50]. Comparison of results is shown for base fluid (water) and nanofluids. Visualization of heat flows would be demonstrated for both of base fluid and water to justify enhancement of heat transfer for various nanofluids. Quantitative comparison of heat transfer rates are done based on local and average Nusselt numbers.

2. Mathematical formulation and simulation

2.1. Velocity and temperature distributions

Present study is based on natural convection within square cavities with various types of wall heating as shown in Fig. 1. The computational domain is two dimensional as shown in Fig. 1a and b. The fluid within the cavity is a water based nanofluid containing various types of nanoparticles: Cu, Al₂O₃ and TiO₂. The nanofluid is sufficiently dilute with mass fraction ≤ 0.2 such that fluid is considered incompressible and the flow is also assumed to be laminar. The base fluid (water) and the nanofluids are assumed to be in thermal equilibrium and no slip occurs between them. Thermophysical properties of the nanofluid are assumed to be constant except the density variations causing a body force term in the vertical component of momentum equation. The Boussinesq approximation is invoked for the fluid properties due to the variation of density with temperature and the density variation cause a body force in the vertical momentum equation as given below. Therefore, the temperature field is coupled to the flow field via the body force term. Under these assumptions governing equations for steady two-dimensional natural convection flow in the square cavity using conservation of mass, momentum and energy can be written with following dimensionless variables or numbers [27]

$$X = \frac{x}{L}, \quad Y = \frac{y}{L}, \quad U = \frac{uL}{\alpha_f}, \quad V = \frac{vL}{\alpha_f}, \quad \theta = \frac{T - T_c}{T_h - T_c},$$

$$P = \frac{pL^2}{\rho_{nf}\alpha_f^2}, \quad Pr = \frac{\nu_f}{\alpha_f}, \quad Ra = \frac{g\beta_f(T_h - T_c)L^3}{\nu_f\alpha_f} \quad (1)$$

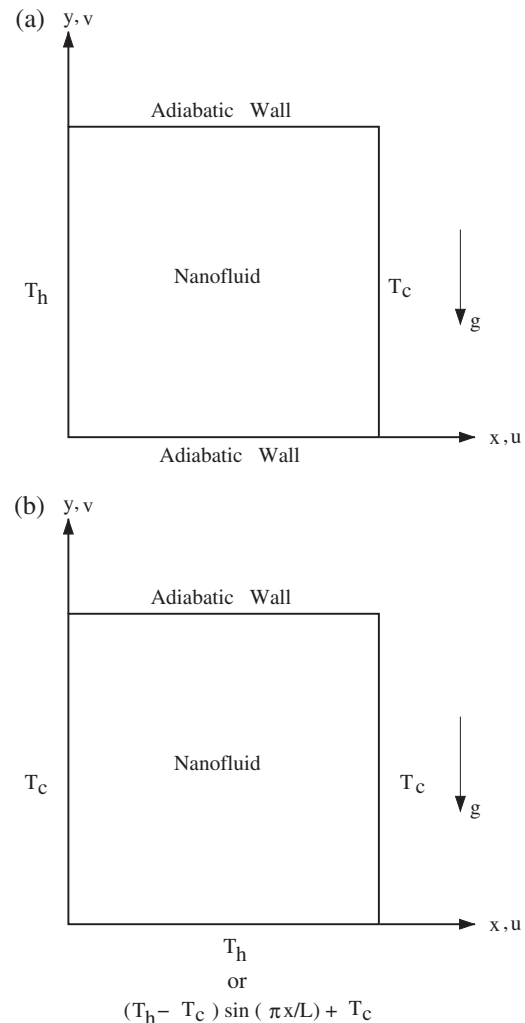


Fig. 1. Schematic of the model system with various boundary conditions. Fig. 1a represents case 1 and Fig. 1b represents case 2.

as:

$$U \frac{\partial U}{\partial X} + V \frac{\partial U}{\partial Y} = -\frac{\partial P}{\partial X} + \frac{\mu_{nf}}{\rho_{nf}\alpha_f} \left(\frac{\partial^2 U}{\partial X^2} + \frac{\partial^2 U}{\partial Y^2} \right), \quad (2)$$

$$U \frac{\partial V}{\partial X} + V \frac{\partial V}{\partial Y} = -\frac{\partial P}{\partial Y} + \frac{\mu_{nf}}{\rho_{nf}\alpha_f} \left(\frac{\partial^2 V}{\partial X^2} + \frac{\partial^2 V}{\partial Y^2} \right) + \frac{(\rho\beta)_{nf}}{\rho_{nf}\beta_f} RaPr\theta, \quad (3)$$

$$U \frac{\partial \theta}{\partial X} + V \frac{\partial \theta}{\partial Y} = \frac{\alpha_{nf}}{\alpha_f} \left(\frac{\partial^2 \theta}{\partial X^2} + \frac{\partial^2 \theta}{\partial Y^2} \right). \quad (4)$$

$$U \frac{\partial \theta}{\partial X} + V \frac{\partial \theta}{\partial Y} = \frac{\alpha_{nf}}{\alpha_f} \left(\frac{\partial^2 \theta}{\partial X^2} + \frac{\partial^2 \theta}{\partial Y^2} \right). \quad (5)$$

In Eq. (1), x and y are the distances measured along the horizontal and vertical directions, respectively; u and v are the velocity components in the x and y directions, respectively; T denotes the temperature; p is the pressure; T_h and T_c are the temperatures at hot and cold walls, respectively; L is the height of the triangular cavity; Pr and Ra denote Prandtl number and Rayleigh number, respectively. The effective properties of nanofluids in Eqs. (2)–(5) are defined in the following manner [27].

The effective density of the nanofluid (ρ_{nf}) is given as

$$\rho_{nf} = (1 - \phi)\rho_f + \phi\rho_p, \quad (6)$$

where ϕ , ρ_f and ρ_p are the solid volume fraction of nanoparticles, density of base fluid and density of nanoparticles, respectively. Thermal diffusivity of the nanofluid is:

$$\alpha_{nf} = \frac{k_{nf}}{(\rho C_p)_{nf}}, \quad (7)$$

where k_{nf} is effective thermal conductivity and the following expression has been used for spherical particles [23,24,51]

$$k_{nf} = k_f \left[\frac{k_p + 2k_f - 2\phi(k_f - k_p)}{k_p + 2k_f + \phi(k_f - k_p)} \right]. \quad (8)$$

Here k_f and k_p are the thermal conductivities of the base fluid and dispersed particles, respectively. In Eq. (7), the heat capacity of the nanofluid is given as

$$(\rho C_p)_{nf} = (1 - \phi)(\rho C_p)_f + \phi(\rho C_p)_p. \quad (9)$$

In a similar manner, the thermal expansion coefficient of the nanofluid can be determined by

$$(\rho\beta)_{nf} = (1 - \phi)(\rho\beta)_f + \phi(\rho\beta)_p. \quad (10)$$

The effective viscosity of the nanofluid may be expressed in the following form based on Brinkman model [52]

$$\mu_{nf} = \frac{\mu_f}{(1 - \phi)^{2.5}}, \quad (11)$$

where μ_f is the viscosity of the base fluid. The thermophysical properties of the base fluid and various solid particles (Copper, TiO₂, Alumina) are given in Table 1.

The boundary conditions for velocities

$$\begin{aligned} U(X, 0) = U(X, 1) = U(0, Y) = U(1, Y) = 0, \\ V(X, 0) = V(X, 1) = V(0, Y) = V(1, Y) = 0. \end{aligned} \quad (12)$$

The boundary conditions for temperature with various cases (see Fig. 1a and b) are

$$\begin{aligned} \theta = 1 \text{ (uniform heating) or } \sin\pi X \\ \text{(non-uniform heating, bottom wall),} \\ \theta = 0 \text{ (for cold wall),} \\ \frac{\partial\theta}{\partial Y} = 0 \text{ (for adiabatic wall).} \end{aligned} \quad (13)$$

It may be noted that uniform heating situation of bottom wall represents isothermal heating of bottom wall which may be induced by flow of saturated steam or phase change material (PCM). Non-uniform or sinusoidal heating may be due to burner heating at the center or due to flow of hot water at the center.

The momentum and energy balance equations (Eqs. (3)–(5)) are solved using the Galerkin finite element method. The continuity equation (Eq. (2)) will be used as a constraint due to mass conservation and this constraint may be used to obtain the pressure distribution. In order to solve Eqs. (3) and (4), we use the penalty finite element method where the pressure P is eliminated by a penalty parameter γ and the incompressibility criteria given by Eq. (2) which results in

$$P = -\gamma \left(\frac{\partial U}{\partial X} + \frac{\partial V}{\partial Y} \right). \quad (14)$$

Table 1
Thermophysical properties of base fluid (pure water) and nanoparticles [27,29].

| Properties | Pure water | Cu | Alumina | TiO ₂ |
|---|---------------------|-----------------------|-----------------------|----------------------|
| C_p (J kg ⁻¹ K ⁻¹) | 4179 | 385 | 765 | 686.2 |
| k (W m ⁻¹ K ⁻¹) | 0.613 | 401 | 40 | 8.9538 |
| ρ (kg m ⁻³) | 997.1 | 8933 | 3970 | 4250 |
| β (K ⁻¹) | 21×10^{-5} | 1.67×10^{-5} | 0.85×10^{-5} | 0.9×10^{-5} |

The continuity equation (Eq. (2)) is automatically satisfied for large values of γ . Typical values of γ that yield consistent solutions are 10^7 . Using Eq. (14), the momentum balance equations (Eqs. (3) and (4)) reduce to

$$U \frac{\partial U}{\partial X} + V \frac{\partial U}{\partial Y} = \gamma \frac{\partial}{\partial X} \left(\frac{\partial U}{\partial X} + \frac{\partial V}{\partial Y} \right) + \frac{\mu_{nf}}{\rho_{nf} \alpha_f} \left(\frac{\partial^2 U}{\partial X^2} + \frac{\partial^2 U}{\partial Y^2} \right) \quad (15)$$

and

$$U \frac{\partial V}{\partial X} + V \frac{\partial V}{\partial Y} = \gamma \frac{\partial}{\partial Y} \left(\frac{\partial U}{\partial X} + \frac{\partial V}{\partial Y} \right) + \frac{\mu_{nf}}{\rho_{nf} \alpha_f} \left(\frac{\partial^2 V}{\partial X^2} + \frac{\partial^2 V}{\partial Y^2} \right) + \frac{(\rho\beta)_{nf}}{\rho_{nf} \beta_f} RaPr\theta. \quad (16)$$

The system of Eqs. (5), (15) and (16) with boundary conditions is solved by using Galerkin finite element method ([53]). Expanding the velocity components (U, V) and temperature (θ) using basis set $\{\Phi_k\}_{k=1}^N$ as,

$$\begin{aligned} U &\approx \sum_{k=1}^N U_k \Phi_k(X, Y), \quad V \approx \sum_{k=1}^N V_k \Phi_k(X, Y), \quad \text{and} \\ \theta &\approx \sum_{k=1}^N \theta_k \Phi_k(X, Y) \end{aligned} \quad (17)$$

for

$$0 \leq X, \quad Y \leq 1,$$

the Galerkin finite element method yields the following nonlinear residual equations for Eqs. (15), (16) and (5), respectively, at nodes of internal domain Ω :

$$\begin{aligned} R_i^{(1)} = \sum_{k=1}^N U_k \int_{\Omega} \left[\left(\sum_{k=1}^N U_k \Phi_k \right) \frac{\partial \Phi_k}{\partial X} + \left(\sum_{k=1}^N V_k \Phi_k \right) \frac{\partial \Phi_k}{\partial Y} \right] \Phi_i dXdY \\ + \gamma \left[\sum_{k=1}^N U_k \int_{\Omega} \frac{\partial \Phi_i}{\partial X} \frac{\partial \Phi_k}{\partial X} dXdY + \sum_{k=1}^N V_k \int_{\Omega} \frac{\partial \Phi_i}{\partial Y} \frac{\partial \Phi_k}{\partial Y} dXdY \right] \\ + \frac{\mu_{nf}}{\rho_{nf} \alpha_f} \sum_{k=1}^N U_k \int_{\Omega} \left[\frac{\partial \Phi_i}{\partial X} \frac{\partial \Phi_k}{\partial X} + \frac{\partial \Phi_i}{\partial Y} \frac{\partial \Phi_k}{\partial Y} \right] dXdY \end{aligned} \quad (18)$$

$$\begin{aligned} R_i^{(2)} = \sum_{k=1}^N V_k \int_{\Omega} \left[\left(\sum_{k=1}^N U_k \Phi_k \right) \frac{\partial \Phi_k}{\partial X} + \left(\sum_{k=1}^N V_k \Phi_k \right) \frac{\partial \Phi_k}{\partial Y} \right] \Phi_i dXdY \\ + \gamma \left[\sum_{k=1}^N U_k \int_{\Omega} \frac{\partial \Phi_i}{\partial Y} \frac{\partial \Phi_k}{\partial X} dXdY + \sum_{k=1}^N V_k \int_{\Omega} \frac{\partial \Phi_i}{\partial Y} \frac{\partial \Phi_k}{\partial Y} dXdY \right] \\ + \frac{\mu_{nf}}{\rho_{nf} \alpha_f} \sum_{k=1}^N V_k \int_{\Omega} \left[\frac{\partial \Phi_i}{\partial X} \frac{\partial \Phi_k}{\partial X} + \frac{\partial \Phi_i}{\partial Y} \frac{\partial \Phi_k}{\partial Y} \right] dXdY \\ - \frac{(\rho\beta)_{nf}}{\rho_{nf} \beta_f} RaPr \int_{\Omega} \left(\sum_{k=1}^N \theta_k \Phi_k \right) \Phi_i dXdY \end{aligned} \quad (19)$$

and

$$\begin{aligned} R_i^{(3)} = \sum_{k=1}^N \theta_k \int_{\Omega} \left[\left(\sum_{k=1}^N U_k \Phi_k \right) \frac{\partial \Phi_k}{\partial X} + \left(\sum_{k=1}^N V_k \Phi_k \right) \frac{\partial \Phi_k}{\partial Y} \right] \Phi_i dXdY \\ + \frac{\alpha_{nf}}{\alpha_f} \sum_{k=1}^N \theta_k \int_{\Omega} \left[\frac{\partial \Phi_i}{\partial X} \frac{\partial \Phi_k}{\partial X} + \frac{\partial \Phi_i}{\partial Y} \frac{\partial \Phi_k}{\partial Y} \right] dXdY \end{aligned} \quad (20)$$

Bi-quadratic basis functions with three point Gaussian quadrature is used to evaluate the integrals in the residual equations. In Eqs. (18) and (19), the second term containing the penalty parameter (γ) are evaluated with two point Gaussian quadrature (reduced integration penalty formulation, Reddy [53]). The non-linear

residual equations (18)–(20) are solved using Newton–Raphson procedure to determine the coefficients of the expansions in Eq. (17). The detailed solution procedure may be found in earlier works [50,54],

2.2. Streamfunction and heatfunction

The fluid motion is displayed using the streamfunction ψ obtained from velocity components U and V . The relationships between streamfunction, ψ [55] and velocity components for two dimensional flows are

$$U = \frac{\partial \psi}{\partial Y} \quad \text{and} \quad V = -\frac{\partial \psi}{\partial X}, \quad (21)$$

which yield a single equation

$$\frac{\partial^2 \psi}{\partial X^2} + \frac{\partial^2 \psi}{\partial Y^2} = \frac{\partial U}{\partial Y} - \frac{\partial V}{\partial X}. \quad (22)$$

Using the above definition of the streamfunction, the positive sign of ψ denotes anti-clockwise circulation and the clockwise circulation is represented by the negative sign of ψ . Expanding the streamfunction (ψ) using the basis set $\{\Phi\}$ as $\psi = \sum_{k=1}^N \psi_k \Phi_k(X, Y)$ and the relation for U and V from Eq. (17), the Galerkin finite element method yields the following linear residual equations for Eq. (22).

$$R_i^s = \sum_{k=1}^N \psi_k \int_{\Omega} \left[\frac{\partial \Phi_i}{\partial X} \frac{\partial \Phi_k}{\partial X} + \frac{\partial \Phi_i}{\partial Y} \frac{\partial \Phi_k}{\partial Y} \right] dXdY - \int_{\Gamma} \Phi_i \mathbf{n} \cdot \nabla \psi \, d\Gamma + \sum_{k=1}^N U_k \int_{\Omega} \Phi_i \frac{\partial \Phi_k}{\partial Y} dXdY - \sum_{k=1}^N V_k \int_{\Omega} \Phi_i \frac{\partial \Phi_k}{\partial X} dXdY \quad (23)$$

The no-slip condition is valid at all boundaries as there is no cross flow, hence $\psi = 0$ is used as residual equations at the nodes for the boundaries. The bi-quadratic basis function is used to evaluate the integrals in Eq. (23) and ψ 's are obtained by solving the N linear residual Eq. (23).

The heat flow within the enclosure is displayed using the heatfunction Π obtained from conductive heat fluxes $(-\frac{\partial \theta}{\partial X}, -\frac{\partial \theta}{\partial Y})$ as well as convective heat fluxes $(U\theta, V\theta)$. The heatfunction satisfies the steady energy balance equation (Eq. (5)) [37] such that

$$\frac{\partial \Pi}{\partial Y} = U\theta - \frac{\alpha_{nf}}{\alpha_f} \frac{\partial \theta}{\partial X}, \quad -\frac{\partial \Pi}{\partial X} = V\theta - \frac{\alpha_{nf}}{\alpha_f} \frac{\partial \theta}{\partial Y}, \quad (24)$$

which yield a single equation

$$\frac{\partial^2 \Pi}{\partial X^2} + \frac{\partial^2 \Pi}{\partial Y^2} = \frac{\partial}{\partial Y}(U\theta) - \frac{\partial}{\partial X}(V\theta). \quad (25)$$

Using the above definition of the heatfunction, the positive sign of Π denotes anti-clockwise heat flow and the clockwise heat flow is represented by the negative sign of Π . Expanding the heatfunction (Π) using the basis set $\{\Phi\}$ as $\Pi = \sum_{k=1}^N \Pi_k \Phi_k(X, Y)$ and the relation for U , V and θ from Eq. (17), the Galerkin finite element method yields the following linear residual equations for Eq. (25).

$$R_i^h = \sum_{k=1}^N \Pi_k \int_{\Omega} \left[\frac{\partial \Phi_i}{\partial X} \frac{\partial \Phi_k}{\partial X} + \frac{\partial \Phi_i}{\partial Y} \frac{\partial \Phi_k}{\partial Y} \right] dXdY - \int_{\Gamma} \Phi_i \mathbf{n} \cdot \nabla \Pi \, d\Gamma + \sum_{k=1}^N U_k \int_{\Omega} \left(\sum_{k=1}^N \theta_k \Phi_k \right) \Phi_i \frac{\partial \Phi_k}{\partial Y} dXdY + \sum_{k=1}^N \theta_k \times \int_{\Omega} \left(\sum_{k=1}^N U_k \Phi_k \right) \Phi_i \frac{\partial \Phi_k}{\partial Y} dXdY - \sum_{k=1}^N V_k \int_{\Omega} \left(\sum_{k=1}^N \theta_k \Phi_k \right) \Phi_i \times \frac{\partial \Phi_k}{\partial X} dXdY - \sum_{k=1}^N \theta_k \int_{\Omega} \left(\sum_{k=1}^N V_k \Phi_k \right) \Phi_i \frac{\partial \Phi_k}{\partial X} dXdY. \quad (26)$$

The residual equation (Eq. (26)) is further supplemented with various Dirichlet and Neumann boundary conditions in order to obtain a unique solution of Eq. (25). Neumann boundary conditions for Π are obtained for isothermal (hot or cold) or sinusoidally heated wall as derived from Eq. (24) and the normal derivatives $(\mathbf{n} \cdot \nabla \Pi)$ are specified as follows:

(a) for bottom wall

$$\mathbf{n} \cdot \nabla \Pi = 0 \quad (\text{isothermal heating}) \\ = \frac{\alpha_{nf}}{\alpha_f} \pi \cos \pi X \quad (\text{sinusoidal heating}) \quad (27)$$

and

(b) for vertical wall

$$\mathbf{n} \cdot \nabla \Pi = 0 \quad (\text{isothermal heating or cooling}) \quad (28)$$

The top insulated wall may be represented by Dirichlet boundary condition as obtained from Eq. (24) which is simplified into $\frac{\partial \Pi}{\partial X} = 0$ for an adiabatic wall. A reference value of Π is assumed as 0 at $X = 0$, $Y = 1$ and hence $\Pi = 0$ is valid for $Y = 1$, $\forall X$. For case 1 (Fig. 1a), $\Pi = \frac{\alpha_{nf}}{\alpha_f} \overline{Nu}_s$ is obtained from Eq. (24) at $X = 0$, $Y = 0$ (adiabatic wall). The boundary conditions for non-adiabatic walls of case 2 (Fig. 1b) are given above in Eqs. (27) and (28).

It may be noted that, the unique solution of Eq. (25) is strongly dependent on the non-homogeneous Dirichlet conditions. Most of earlier works [42,48] are limited within two adiabatic walls where Dirichlet boundary condition is either 0 or Nu at the adiabatic walls. For the situations of differential heating of walls (case 2; Fig. 1b), Dirichlet conditions for Π have been obtained based on heat flux balance i.e., the total heat gained by the cold wall should be equal to the total heat loss from the hot wall.

$$\Pi = \overline{Nu}_s, \quad X = 0, \quad Y = 0 \\ = -\overline{Nu}_s, \quad X = 1, \quad Y = 0 \quad (29)$$

It may be noted that \overline{Nu}_s and \overline{Nu}_b are average Nusselt numbers for left/right wall and bottom wall, respectively. The details on evaluation of Nusselt numbers for various non-adiabatic walls are given in next section.

2.3. Nusselt number

The heat transfer coefficient in terms of the local Nusselt number (Nu) is defined by

$$Nu = \frac{hL}{k_f} = -\left(\frac{k_{nf}}{k_f}\right) \frac{\partial \theta}{\partial n}, \quad (30)$$

where h is the convection heat transfer coefficient and n denotes the normal direction on a plane. The local Nusselt numbers at the bottom wall (Nu_b) and at the side wall (Nu_s) are defined as

$$Nu_b = \left(\frac{k_{nf}}{k_f}\right) \left| -\sum_{i=1}^9 \theta_i \frac{\partial \Phi_i}{\partial Y} \right| \quad (31)$$

and

$$Nu_s = \left(\frac{k_{nf}}{k_f}\right) \left| -\sum_{i=1}^9 \theta_i \frac{\partial \Phi_i}{\partial X} \right|. \quad (32)$$

The average Nusselt numbers at the bottom and side walls are

$$\overline{Nu}_b = \frac{\int_0^1 Nu_b dX}{X|_0^1} = \int_0^1 Nu_b dX \quad (33)$$

and

$$\overline{Nu}_s = \frac{\int_0^1 Nu_s dY}{Y|_0^1} = \int_0^1 Nu_s dY. \quad (34)$$

3. Results and discussion

3.1. Numerical tests

3.1.1. Streamlines and isotherms

The computational domain consists of 20×20 bi-quadratic elements which correspond to 41×41 grid points. The bi-quadratic elements with lesser number of nodes smoothly capture the non-linear variations of the field variables which are in contrast with finite difference/finite volume solutions available in the literature [27,28]. In order to assess the accuracy of the numerical procedure, we have carried out computations based on the grid size (41×41) for a square enclosure filled with air ($Pr = 0.71$) subjected to hot left wall and cold right wall in presence of insulated horizontal walls at $Ra = 10^5$. It is found that the average Nusselt number (\overline{Nu}) based on finite element solution is 4.62 which is in good agreement with earlier reported results [29,56–58]. Present work based on bi-quadratic elements with lesser number of nodes (41×41) smoothly capture the non-linear variations of the field variables which are in contrast with finite difference/finite volume solutions available in the literature [27,28]. It may be noted that a recent work [28] based on finite volume method involved 51×51 nodes for the converged solution.

In the current investigation, Gaussian quadrature based finite element method provides smooth solutions in the computational domain including the corner regions with singularities for isothermally hot bottom wall and cold isothermal side walls as evaluation of residuals depends on interior Gauss points and thus the effect of corner nodes are less pronounced in the final solution. Current solution scheme produces grid invariant results as discussed in our previous articles [50,54]. The convergences tests have been carried out for all present cases and it is observed that 41×41 computational grids are adequate for smooth solutions.

3.1.2. Heatlines

Simulations with heatfunctions strongly depend on non-homogeneous Dirichlet boundary conditions. Although the homogeneous Neumann boundary conditions are valid (Eq. (28)) for the isothermal walls, but the uniqueness of the solution of Eq. (25) depends on Dirichlet conditions. For case 1 with isothermal side walls and adiabatic horizontal walls, $\Pi = 0$ is assumed at the bottom wall ($Y = 0, \forall X$) and consequently, $\Pi = \frac{\alpha_{nf}}{\alpha_f} \overline{Nu}$ (where \overline{Nu} is the average Nusselt number) is obtained for the top wall ($Y = 1, \forall X$). In general, the Dirichlet boundary conditions for Π of adiabatic walls are naturally obtained for the case 1 via integrating Eq. (24). The sign of heatfunction needs special mention. The solution of heatfunction (Poisson equation) is strongly dependent on non-homogeneous Dirichlet boundary condition ($\Pi = \frac{\alpha_{nf}}{\alpha_f} \overline{Nu}$) and the sign of heatfunction is governed by the sign of 'non-homogeneous' Dirichlet condition. It is observed that the sign of heatfunction is positive (as also assumed in the earlier work [37]) near the top wall and the sign is negative in the core where the heatfunctions denote strong convective heat transfer for case 1. It may be noted that signs of streamfunction and heatfunction are identical for the convection dominated heat flows as also seen in Fig. 2 and Fig. 3a–c. A detailed explanation for this situation may be found in earlier articles [37,48].

3.2. Case 1: isothermal side walls and adiabatic vertical walls

Figs. 2 and 3a–c illustrate isotherms, streamlines and heatlines for water and Cu–Water nanofluids for various volume fractions of nanoparticles for a range of Ra ($Ra = 10^3 - 10^5$). Test cases with Cu–Water nanofluid ($\phi = 0.1$) for a range of Ra were also shown in an earlier article [28] and present simulation studies (Fig. 2)

show good agreement with previous work [28]. However, heat flow visualization via heatlines for natural convection within nanofluids are yet to appear in literature and present work initiates the analysis of heating pattern via heat flow visualization using heat-functions (Π).

Fig. 2a–c show distributions for dilute Cu–Water nanofluids ($\phi = 0.1$). The distributions are also shown for pure water for comparisons. Effect of nanofluid is observed for all ranges of Ra . It is observed that the shapes of the flow circulation cells are affected by nanofluids. Flow circulations with larger intensity is observed for water based on the fact that the diameter of specific streamline cell for water is larger than that for nanofluid at a constant value of ψ as also reported in an earlier work [28]. At low Ra , isotherms are almost parallel whereas boundary layer is found to be formed along the side walls at higher Ra . Fig. 2a shows that the heatlines are almost parallel for nanofluids whereas heatline circulation cell is observed for water at the center at $Ra = 10^3$. The heatline circulation cell further indicates dominant convective heat flow trajectories for water. It is found that the diameter of flow circulation cell for water is bigger than that for nanofluid corresponding to a specific streamfunction, and consequently the closed loop heatline cells are observed for water at the center. Note that, the diameter of streamline cell for nanofluid (first solid contour line near the center) is much smaller than the diameter of streamline cell for water (second dotted contour line near the center) at $|\psi| = 0.9$. Closed loop heatline cells signify convection dominance and isotherms are much distorted at the center for water. On the other hand, the heat flow trajectories or heatlines are almost parallel for nanofluids and isotherms are found as almost parallel vertical lines. Parallel heatlines further indicate that convective heat transport is reduced significantly in presence of nanofluids for $Ra = 10^3$. It may be noted that flow is due to viscous effect at low Ra and addition of nanoparticles turns the fluid more viscous resulting in less intense flow for nanoparticles. Suppression of convection with nanofluids for $\phi = 0.1$ were also reported by Ho et al. [23]. However, as a first attempt, current work based on heatline concept clearly demonstrates the suppression of convection due to nanofluids at $Ra = 10^3$. It is interesting to observe that the isotherms near the side walls are almost identical for water and nanofluid ($\phi = 0.1$). However, the average Nusselt number for nanofluid is influenced significantly as the average Nusselt number is the product of thermal conductivity ratio (k_{nf}/k_f) and temperature gradient. In general, the thermal conductivity ratio is quite high even with smaller values of ϕ . Therefore, significant deviations of heatlines are observed near the side walls for water and nanofluids even though isotherms look almost identical for water and nanofluid. It may also be noted that, the normal heat flux or local Nusselt number is directly proportional to gradient of heatfunction across the wall (Eq. (30)). It is observed that the heatlines corresponding to higher magnitudes for nanofluids coincide with heatlines corresponding to smaller magnitudes for water. Note that, the maximum value of heatfunction ($|\Pi|_{max}$) for water is 1.12 and that for nanofluid ($\phi = 0.1$) is 1.41 at $Y = 1, \forall X$. Therefore, heatlines clearly illustrate that normal heat flux or local Nusselt number for nanofluid is larger than for water at any point of the wall.

Fig. 2b shows that convective cells for heatlines appear both for water and nanofluids. It is important to note that the intensity of fluid motion is stronger at the center for $Ra = 10^4$. Therefore, more intense convective heat flow at the center occurs for both water and nanofluid. At higher Ra , streamlines and heatlines exhibit similar qualitative profiles. It is interesting to observe that the diameters of flow circulation cells are almost identical for water and nanofluid (see the second column of Fig. 2b). Heatlines pattern show that significant convective heat flow occurs for nanofluids at $Ra = 10^4$ which contrasts previous case with $Ra = 10^3$. Slightly bigger diameter of convection heatline cells are observed at center

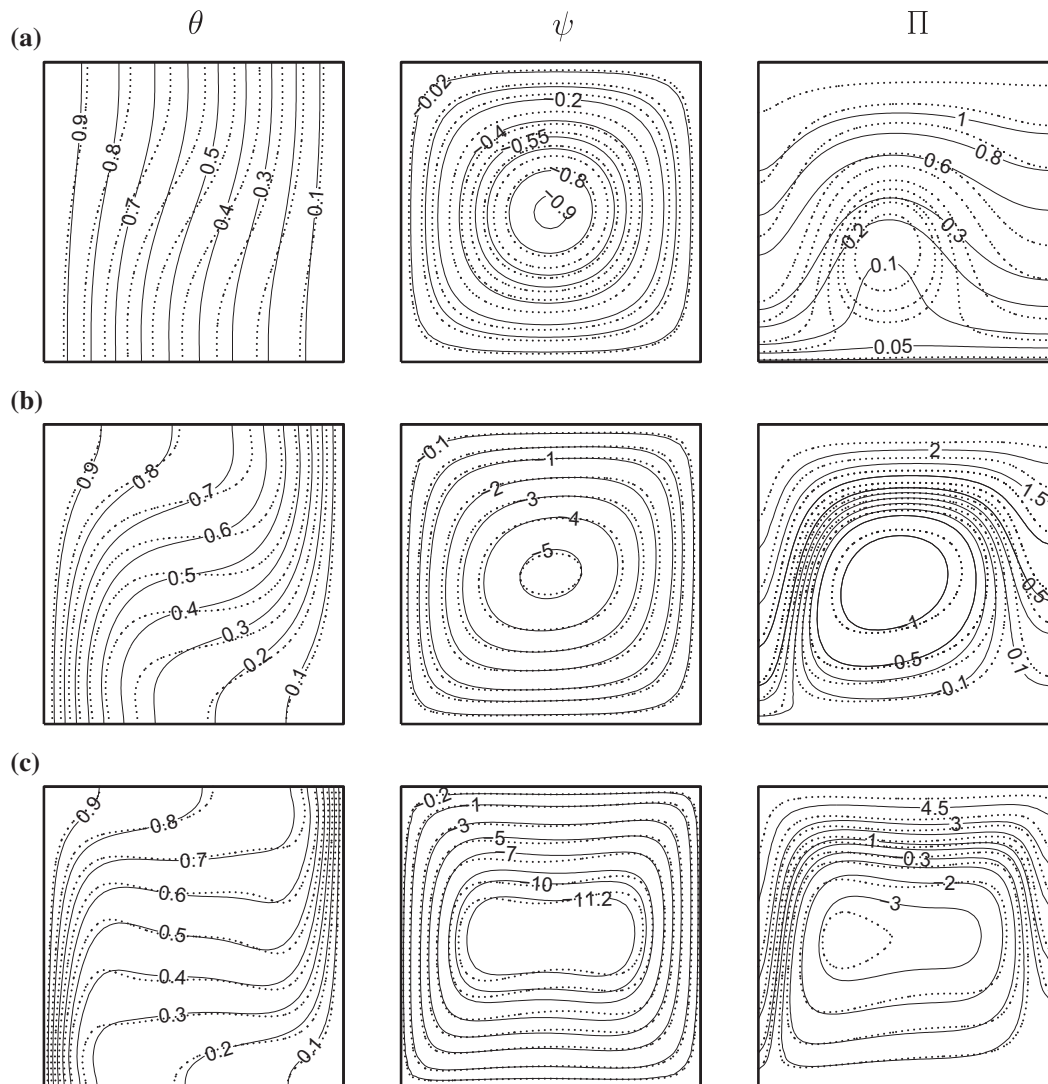


Fig. 2. Temperature (θ), streamfunction (ψ) and heatfunction (Π) contours for isothermally hot left and cold right walls of Cu–Water nanofluids (benchmark problem) for $\phi = 0.1$ with (a) $Ra = 10^3$, (b) $Ra = 10^4$ and (c) $Ra = 10^5$, water and –, nanofluid. The labels of contours are shown for solid lines (–) and the contours with dotted line (...

for water and thus the significant difference in isotherms are observed at the center. Similar to previous case with $Ra = 10^3$, heatline with larger magnitude of Π for nanofluid coincides with heatline with a smaller magnitude of Π of water along the side wall. It is interesting to observe that heatlines with identical magnitudes of heatfunctions coincide near the bottom portion of side wall and this is consistent with merging of isotherms for nanofluid and water at the bottom portion. It may be noted that, $(|\Pi|_{max})$ for water is 2.28 and that for nanofluid ($\phi = 0.1$) is 2.52 at $Y = 1$, $\forall X$.

Fig. 2c shows that significant convection occurs for nanofluids especially at the center as seen from streamlines and heatlines at $Ra = 10^5$. It may be noted that the maximum value of streamfunction ($|\psi|_{max}$) is 12.4 with nanofluid whereas $|\psi|_{max}$ is 11.03 with water. It is interesting to observe that the streamline with $\psi = -11.2$ for nanofluid almost overlaps with the streamline with $\psi = -10$ for water. The more intense convection due to nanofluid at higher Ra is due to dominant effect of buoyancy force for nanofluid based on the values of ρ and β . Also, at higher Ra the buoyancy force dominates the viscous force. Note that, the gradient of heatfunction is directly proportional to velocity and temperature for the convective heat transport (see Eq. (24)) and therefore a sharp difference in heatfunction occurs at the center of the cavity

for nanofluids and water. It is observed that the diameter as well as size of the heatline cell for nanofluid is quite larger than that for water corresponding $\Pi = -3$ at the center. Similar to cases with smaller Ra , the heatlines with larger magnitudes of Π for nanofluid coincide those with smaller magnitudes of Π for water especially near the top portion of side walls. It is also found that dense heatlines occur at the bottom portion of the left wall both for nanofluid and water and highly dense isotherms occur in that zone. It may be noted that the deviations of heatlines are quite less near the bottom portion of side walls as the isotherms are almost identical for both nanofluids and water. Overall, it is observed that $|\Pi|_{max}$ for nanofluid is 5.41 whereas that is 4.84 for water.

Fig. 3a–c illustrate isotherms, streamlines and heatlines for Cu–Water nanofluids ($\phi = 0.2$) and pure water. Fig. 3a shows that significant deviations of isotherms occur at the central zone. It is interesting to observe that the isotherms are parallel vertical lines in presence of nanofluids at low Ra ($Ra = 10^3$). Further, conduction dominant heat transport within nanofluids may be confirmed with less intense streamfunctions as seen in Fig. 3a. It is interesting to observe that the flow intensity is considerably reduced with higher fraction of particles ($\phi = 0.2$) in nanofluids and the reduced flow intensity of nanofluids is due to larger viscous effect at higher solid

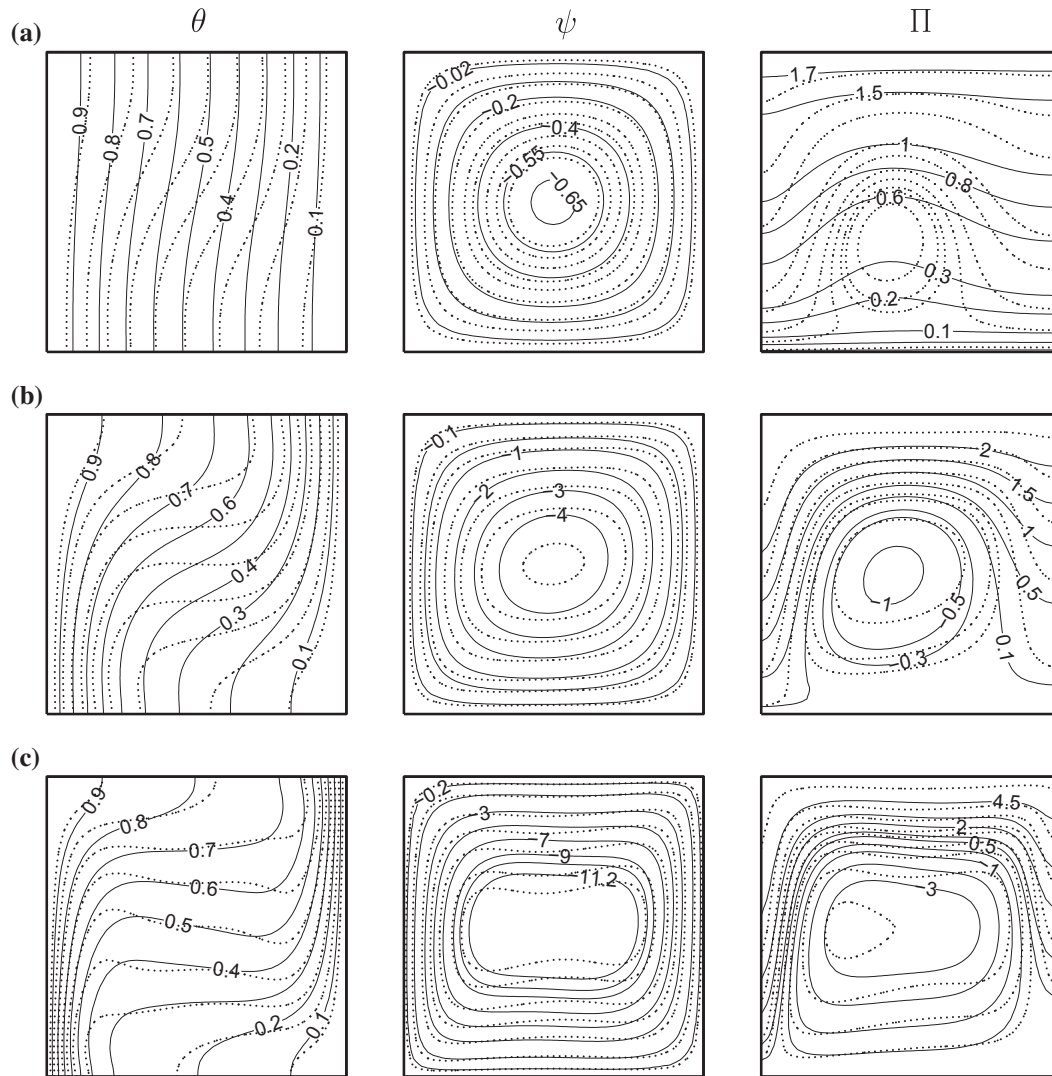


Fig. 3. Temperature (θ), streamfunction (ψ) and heatfunction (Π) contours for isothermally hot left and cold right walls of Cu–Water nanofluids (benchmark problem) for $\phi = 0.2$ with (a) $Ra = 10^3$, (b) $Ra = 10^4$ and (c) $Ra = 10^5$. . . , water and – , nanofluid. The labels of contours are shown for solid lines (–) and the contours with dotted line (.) and solid line (–) are shown for specific labels.

fraction. Note that, the maximum value of streamfunction ($|\psi|_{max}$) is found as 1.17 for pure water whereas $|\psi|_{max}$ are 0.92 and 0.68 for $\phi = 0.1$ and 0.2 , respectively. The convective heat transport is more pronounced at the central zone for both Cu–Water nanofluid and water based on heatlines. However, it is important to note the significant effect on addition of nanoparticles as can be seen from heatlines with lesser degree of plateau compared to those as seen in Fig. 2a. It is found that closed loop heatlines at the central zone occur for pure water whereas the heatlines are parallel for Cu–Water nanofluid at $Ra = 10^3$ (see Fig. 3a). Significant deviations of heatlines are observed along the vertical walls based on the values of k_{nf}/k_f although there is a difference in isotherms with lesser degree for nanofluids and water near the vertical walls. The enhancement of heat transfer is largely pronounced throughout the side wall as heatlines with larger values of Π for nanofluid merge with those with smaller magnitudes. It is interesting to observe that heatline with $\Pi = 1.7$ for nanofluid coincides with $\Pi = 1$ at the top portion of the right wall.

Fig. 3b illustrates the distributions for $Ra = 10^4$. The deviations of isotherms are significant at the central regime as the flow is suppressed for Cu–Water nanofluids. It is interesting to observe that $|\psi|_{max}$ is 5.2 and 4.9 for water and nanofluid ($\phi = 0.2$), respectively.

The heatlines further illustrate that closed loop heatlines occur at the central zone for both water and nanofluids. Thus, convective heat transport is found to be dominant at the center for both water and nanofluids. It is important to note that still the convective heat flow is more intense at the center for water based on diameter of the convective heatline cell size. Therefore isotherms are more twisted for water compared to Cu–Water nanofluid at the core. Significant deviations of heatlines are observed along the side walls and isotherms for water and nanofluid are also not identical.

The heating and flow characteristics have been significantly influenced for $\phi = 0.2$ at high Ra (see Fig. 3c). Based on similar discussion for Fig. 2c, the buoyancy force is more dominant over viscous force for nanofluids with $\phi = 0.2$ compared to $\phi = 0.1$. It may be noted that, $|\psi|_{max}$ is 13.7 for $\phi = 0.2$ whereas those are 11.03 for pure water and 12.4 for $\phi = 0.1$. Due to significant convection near the central zone, the isotherms show similar qualitative trend for water and nanofluids. The dominant convective heat transport via closed loop heatline cells is observed for both water and nanofluids. It is interesting to observe that the more intense convective heat transport occurs for nanofluids near the core as shown with heatlines and this is a consequence of more intense flow intensity within nanofluids. It may be noted that, the diameter of the

heatline cell for water is much smaller than that for nanofluid ($\phi = 0.2$) corresponding to $\Pi = -3$ at the center of the cavity. The distributions of heatline show that dense heatlines occur near the bottom portion of left vertical wall signifying enhanced heat transport. Similar to previous cases, heatlines with larger Π for nanofluid coincide with heatlines with smaller Π for water near the side walls. It is interesting to observe that heatline with $\Pi = 4.5$ for nanofluid merges with heatline with $\Pi = 3$ for water near the top wall of the cavity. Note that, $|\Pi|_{\max}$ is 5.9 for nanofluid ($\phi = 0.2$) whereas that is 4.84 for water and 5.41 for nanofluid with $\phi = 0.1$ at $Ra = 10^5$.

Fig. 4a demonstrates local Nusselt number at the left wall (Nu_l) vs distance for various solid fractions ($\phi = 0, 0.1$ and 0.2) where upper, middle and bottom panels correspond to $Ra = 10^3, 10^4$ and 10^5 , respectively. Current simulation results agree well with the earlier work [28]. As mentioned earlier, viscous force is more dominant over buoyancy force, and the convection gradually becomes less intense with increase of ϕ at low Ra ($Ra = 10^3$) (see top panel of Fig. 4a). Overall, conductive heat flux is dominant and gradient of Π with nanofluids is larger than that with water along the isothermal wall at small Ra . It may be important to note that both conductivity and viscosity of nanofluid increase with ϕ , and enhancement of conductive heat flux is more pronounced at higher ϕ . Note that, along the left wall, Π varies within 0–1.12 for water whereas for nanofluids, that varies within 0–1.411 and 0–1.839 for $\phi = 0.1$ and 0.2 , respectively. Thus, based on variation of heatfunctions across the wall, Nu_l is the largest for nanofluids with $\phi = 0.2$. Common to all cases, it is observed that Nu_l decreases with distance from the bottom corner and this is based on the fact that large heat transport occurs near the bottom portion of the wall as seen from dense heatlines both for water and nanofluids. It is also interesting to observe that the deviation in magnitudes of Nu_l for water and nanofluids is more near the top portion of the left wall. This is based on the fact that the heatlines with larger Π for nanofluid coincide with heatline with smaller Π for water

especially at top portion of the left wall whereas the difference in magnitudes of Π is less at the bottom portion of the left wall (see Figs. 2a and 3a).

The middle panel of Fig. 4a illustrate the variation of Nu_l vs distance for $Ra = 10^4$. Similar decreasing trend on Nu_l vs distance is observed based on heatlines distributions. Buoyancy force gradually becomes dominant for higher ϕ at a larger Ra and convective heat transport is also found to be significant at higher Ra as seen in Figs. 2b and 3b. Thus enhancement of local heat transfer rates are observed for $\phi = 0.1$ and 0.2 compared to that for water. Enhancement of Nu_l may be also seen from heatfunction variations along the left wall. Note that, Π varies within 0–2.283 for water whereas that varies within 0–2.52 for $\phi = 0.1$ and 0–2.72 for $\phi = 0.2$. Qualitatively similar trend on Nu_l is observed at $Ra = 10^5$ (see bottom panel of Fig. 4a). Enhancement of heat transfer is similarly explained based on dominant convective heat transport and distributions of heatfunctions. The deviation in magnitudes of Nu_l for water and nanofluids ($\phi = 0.2$ is larger at the bottom portion of the left wall and this may also be explained based on the fact that heatlines with larger magnitude of Π for nanofluid coincide with those with similar magnitudes of Π for water.

Fig. 4b shows the variations of average Nusselt number ($\overline{Nu_l}$) vs Rayleigh number for $\phi = 0, 0.1$ and 0.2 . It may be noted that the values of average Nusselt numbers with $\phi = 0$ and 0.1 for $Ra = 10^3, 10^4$ and 10^5 agree well with the earlier data [28]. Due to conduction dominant heat transport, the average Nusselt number is significantly larger for $\phi = 0.2$ compared to that for $\phi = 0.1$ at $Ra = 10^3$. At $Ra = 10^4$, convection gradually becomes dominant for nanofluids and thus, the difference in heat transfer rates (Nu_l and $\overline{Nu_l}$) for various ϕ s are not larger compared to that with $Ra = 10^3$. At high Rayleigh number, the convective heat transport for nanofluids also become significant as seen Fig. 3c. It is found that, the local Nusselt number is much larger for $\phi = 0.2$ along the bottom portion of the left wall compared to that along the

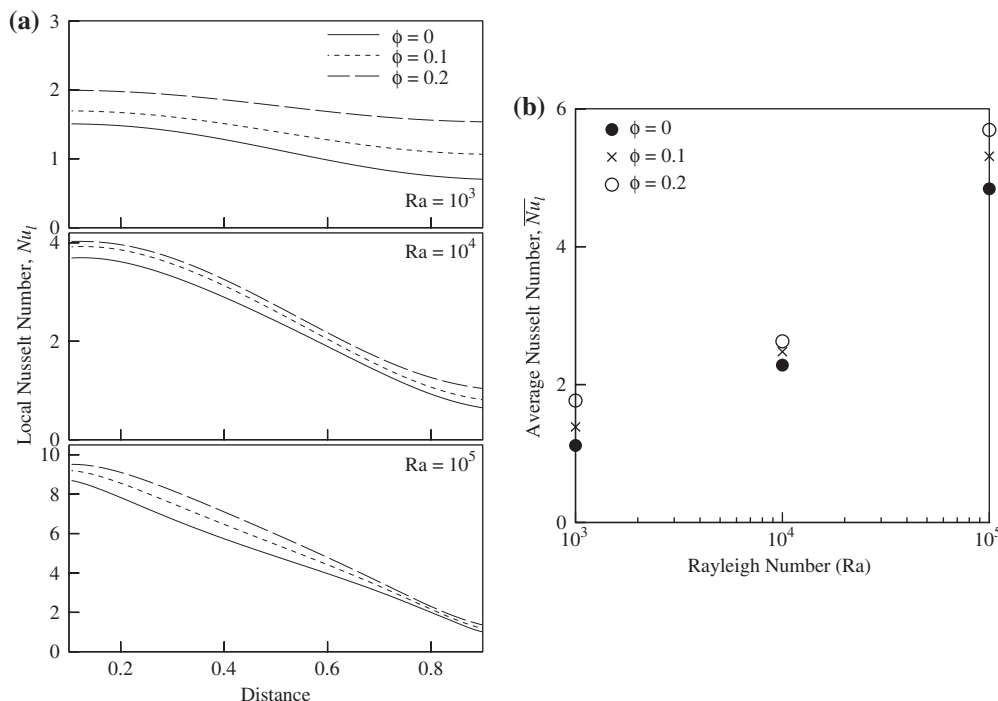


Fig. 4. (a) Local Nusselt number, Nu_l vs distance and (b) Average Nusselt number, Nu_l vs Rayleigh number for various volume fractions (ϕ) of Copper–Water nanofluids in presence of isothermal hot left and cold right walls.

top portion as seen in bottom panel of Fig. 4a. Overall, the average Nusselt number is found to be largely enhanced for $\phi = 0.2$ compared to that for $\phi \leq 0.1$ at $Ra = 10^5$ (Fig. 4b).

3.3. Case 2: uniform and nonuniform heating of bottom wall

Fig. 5a–c illustrate streamfunction, isotherms and heatfunctions for water (dotted lines) and nanofluids (solid lines) with $Ra = 10^3$ in presence of uniform heating of bottom wall and isothermally cold side walls. Comparison of flow and thermal characteristics is shown for water and nanofluids with $\phi = 0.1, 0.15$ and 0.2 . Due to cold vertical walls, fluids rise up from middle portion of the bottom wall and flow down along vertical walls forming two symmetric rolls inside the cavity as denoted by signs of streamfunctions. At $Ra = 10^3$, the magnitudes of streamfunctions are small signifying conduction dominant heat transfer within the cavity and the temperature contours are smooth lines which span the entire cavity. Common to all situations, thermal boundary layer is found to grow at the edge of the bottom corners and larger thickness of boundary layer is found to be seen at the top portion of side wall. It is interesting to observe that thermal boundary layer

thickness at the top portion of side walls is larger for nanofluids and that increases with solid fractions (ϕ). Higher solid fraction corresponds to higher viscosity and less fluid motion at $\phi = 0.2$. Therefore, the large amount of fluid remain cooler along the side walls due to less mobility of the fluid for $\phi = 0.2$ resulting in increase in thermal boundary layer thickness. The temperature distributions are almost identical near the bottom wall of the cavity and it is found that isotherms with $\theta \geq 0.5$ are not influenced by presence of nanofluids for the entire range of ϕ .

Two symmetric flow circulation patterns are observed within the cavity and flow patterns are qualitatively similar for water and nanofluids. As mentioned earlier, viscous effect is more dominant at low Ra and viscosity increases with ϕ resulting in less intense flow at $\phi = 0.2$. Therefore, the flow intensity remains stronger for water at the center of the cavity. Note that, $|\psi|_{max} = 0.20$ for water whereas $|\psi|_{max}$ are 0.138, 0.116 and 0.097 for $\phi = 0.1, 0.15$ and 0.2 , respectively. It is also found that the diameter of flow circulation cell size at the center for water is larger than that with nanofluid ($\phi = 0.1$) corresponding to $|\psi| = 0.1$ (see Fig. 5a). Further, the cell size corresponding to $|\psi| = 0.1$ is reduced for $\phi = 0.15$ (Fig. 5b) and that cell with $|\psi| = 0.1$ disappears for $\phi = 0.2$ (see Fig. 5c). Similarly the diameters

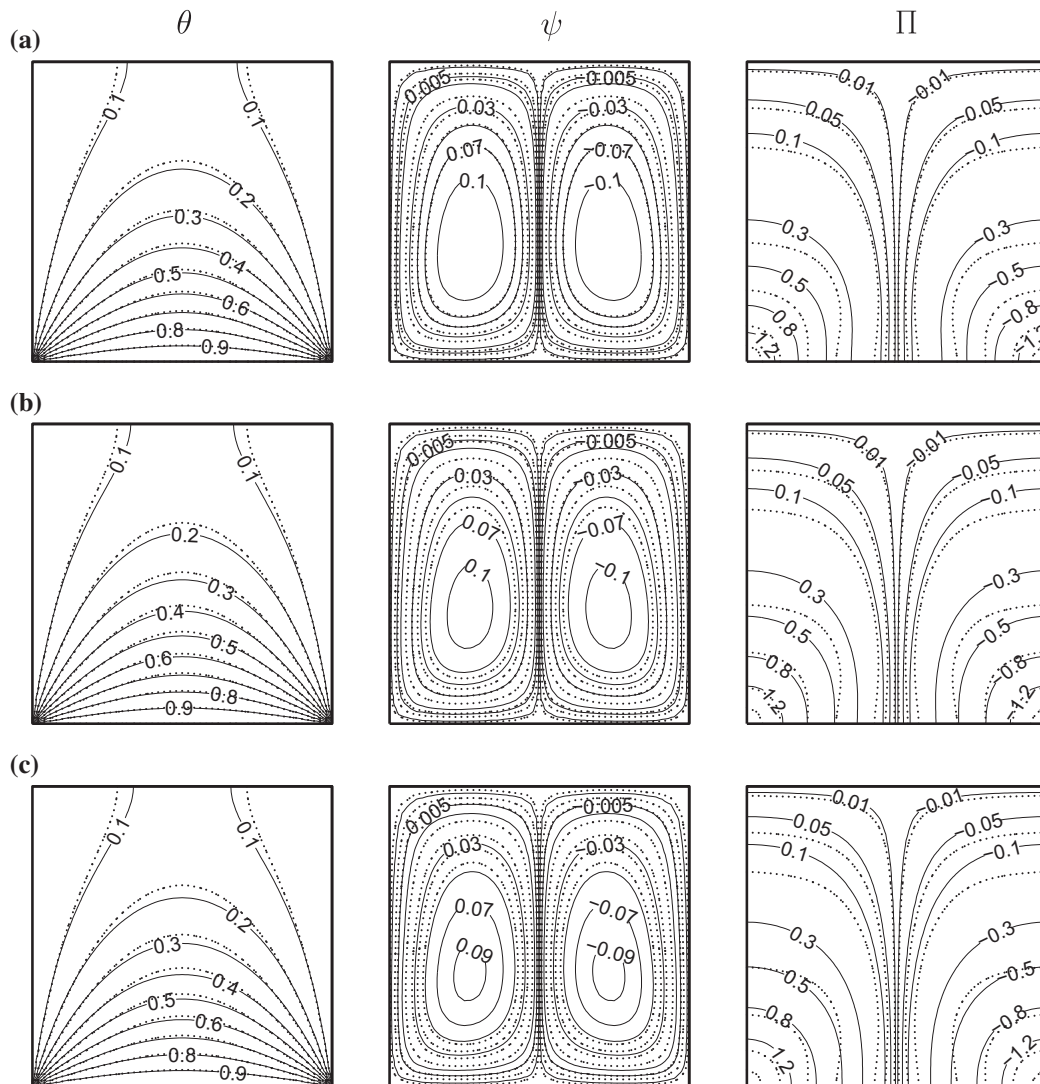


Fig. 5. Temperature (θ), streamfunction (ψ) and heatfunction (Π) contours for isothermally hot bottom and cold side walls of Cu–Water nanofluids ($Ra = 10^3$) with (a) $\phi = 0.1$, (b) $\phi = 0.15$ and (c) $\phi = 0.2$, water and –, nanofluid. The labels of contours are shown for solid lines (–) and the contours with dotted line (...) and solid line (–) are shown for specific labels.

of other cells for water are larger than those with nanofluids corresponding to specific streamfunctions (ψ) except near the wall.

The heatlines in Fig. 5a–c illustrate that the heat flow occurs mainly due to conduction as the heatlines are perpendicular to the cold or hot walls. The two bottom corner edges have infinite heat flux as the cold wall is directly in contact with the hot bottom wall. It may be noted that $\Pi = \overline{Nu}_l = 2.68$ at $X = 0, Y = 0$ and $\Pi = \overline{Nu}_r = -2.68$ at $X = 1, Y = 0$ for water whereas $|\overline{Nu}_l| = |\overline{Nu}_r| = 3.63, 4.20$ and 4.84 for Cu–Water nanofluids with $\phi = 0.1, 0.15$ and 0.2 , respectively. It may also be noted that the signs of heatfunctions are dependent on these two corner boundary conditions. Our sign convention is based on the fact that the heat flow occurs from the hot to cold wall, and the positive heatfunction corresponds to anticlockwise heat flow. It may also be noted that, \overline{Nu} denotes the total or cumulative heat flux at the two bottom corner points and therefore, the magnitudes of heatfunctions decrease from the bottom edges to the central symmetric line where no heat flux condition is also valid due to symmetric boundary conditions for temperature.

It is interesting to observe that, heatline with $\Pi = 0.5$ connects within $X = 0.2$ and $Y = 0.25$ lines implying that more than 50% of the heat flux from the hot wall to cold wall is confined within the

bottom portion of the cold wall. Consequently, the less heat flow occurs near the top portion of the cold walls. Therefore, the thermal boundary layer was found to develop near the bottom edges, and the thickness of boundary layer is larger at the top portion of the cold wall signifying less heat transfer from the hot wall. It may also be noted that as 50% heat energy flows from the regime $0 \leq X \leq 0.2$ and $1 \geq X \geq 0.8$ of the hot wall and the regime near to central regime of the hot wall remain hot as seen from dense heatlines or isotherms near the center of the bottom wall. The heatlines clearly illustrate that the bottom portion of the cold wall receives most of heat energy from the hot wall whereas the top portion of the cavity remains cool due to less transport of heat energy from the bottom wall. It is interesting to note that the fountain of heatlines from the central regime of the bottom wall is not strong enough to reach the regimes of top wall due to weak circulation and conduction dominant heat transfer.

Isotherms for nanofluids and water show similar qualitative trends and the slight difference in magnitudes of isotherms due to nanofluids is observed at top portion of side walls and at top portion of the cavity. Although the deviations of isotherms for nanofluids from those of water are small, heatlines show significant deviations due to enhanced thermal conductivity of nanofluid

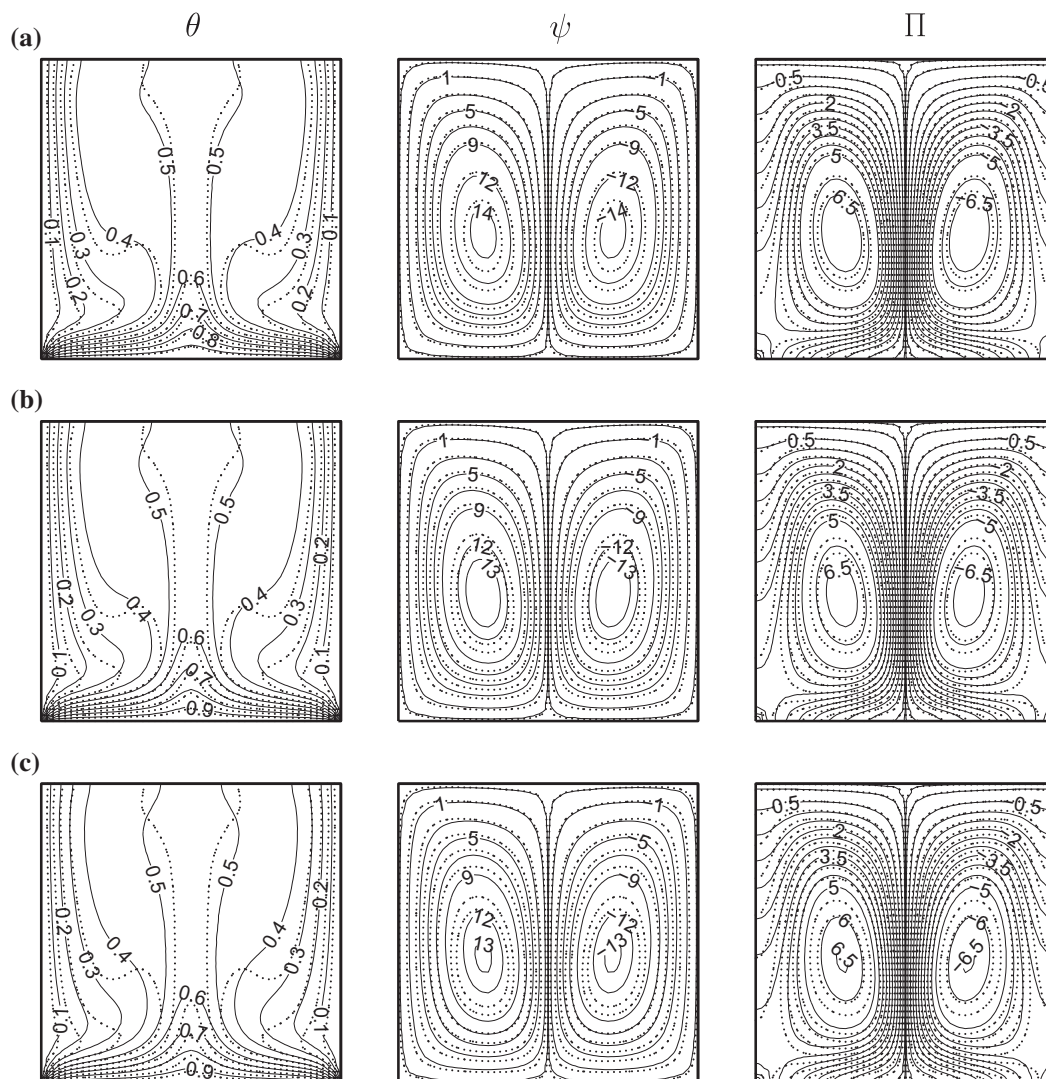


Fig. 6. Temperature (θ), streamfunction (ψ) and heatfunction (Π) contours for isothermally hot bottom and cold side walls of Cu–Water nanofluids ($Ra = 10^5$) with (a) $\phi = 0.1$, (b) $\phi = 0.15$ and (c) $\phi = 0.2$. . . , water and – , nanofluid. The labels of contours are shown for solid lines (–) and the contours with dotted line (...) and solid line (–) are shown for specific labels.

and also, gradient of heatfunction is directly proportional to ratio of thermal diffusivities and normal heat flux (see Eq. (30)). It is observed that heatlines of higher magnitudes for nanofluids coincide with heatlines with smaller magnitudes for water at various locations of side and bottom walls for all solid fractions. The deviations in magnitudes of coinciding heatlines for nanofluids and water are more near the bottom portions of side walls and edges of the bottom wall. The local Nusselt numbers for nanofluids and water are the functions of magnitudes of heatfunctions at particular locations and the detailed analysis will follow later.

Fig. 6a–c illustrate the isotherms, streamlines and heatlines for Cu–Water nanofluids with $\phi = 0.1, 0.15, 0.2$ and $Ra = 10^5$. Qualitatively similar trends in isotherms, streamlines and heatlines are observed for nanofluids and water. It may be important to note that, the viscous effect dominates over buoyancy even at larger Ra for case 2 which contrast case 1 at larger Ra . Common to all nanofluids, the diameter of flow circulation cell for nanofluids is smaller than that for water corresponding to specific values of streamfunctions (Fig. 6). It is interesting to observe that, central flow circulation cell for $\phi = 0.1$ corresponds to $|\psi| = 14$. As ϕ increases to 0.2, the inner circulation cell with $|\psi| = 14$ vanishes, and a smaller flow cell corresponding to $|\psi| = 13$ exists at the

center. Due to enhanced viscous effect and less fluid mobility, the thermal boundary layer thickness along the vertical walls is smaller for water compared to nanofluids with all solid fractions. It is interesting to observe that isotherms corresponding to $\theta = 0.3$ and 0.4 for water coincide with isotherms of $\theta = 0.2$ and 0.3, respectively for nanofluid with $\phi = 0.2$ near the upper portions of side walls (see Fig. 6c). On the other hand, dominant conductive heat transport is observed near the top portion of the central zone where the flow is seen to diverge along two counter-rotating cells. Therefore, the area bounded by isotherms with $\theta = 0.5$ and 0.6 is larger for nanofluids and that area gradually increases with ϕ .

Similar to previous case, the heatlines for water and nanofluids are found to be qualitatively similar. It is interesting to observe that the convective heat transport for water is more intense compared to nanofluids at the center of each heatline circulation zone irrespective of all solid fractions (ϕ). Note that, the size of the cell corresponding to $|II| = 6.5$ is bigger for water than that for nanofluid irrespective of ϕ s whereas the size is gradually reduced with ϕ . Similar trend is observed for the subsequent heatline cells. Consequently, enhanced thermal convection for water results in larger local thermal mixing and area bounded by isotherms with $\theta = 0.4$ and 0.5 is larger at the top portion in each half of the cavity. On the

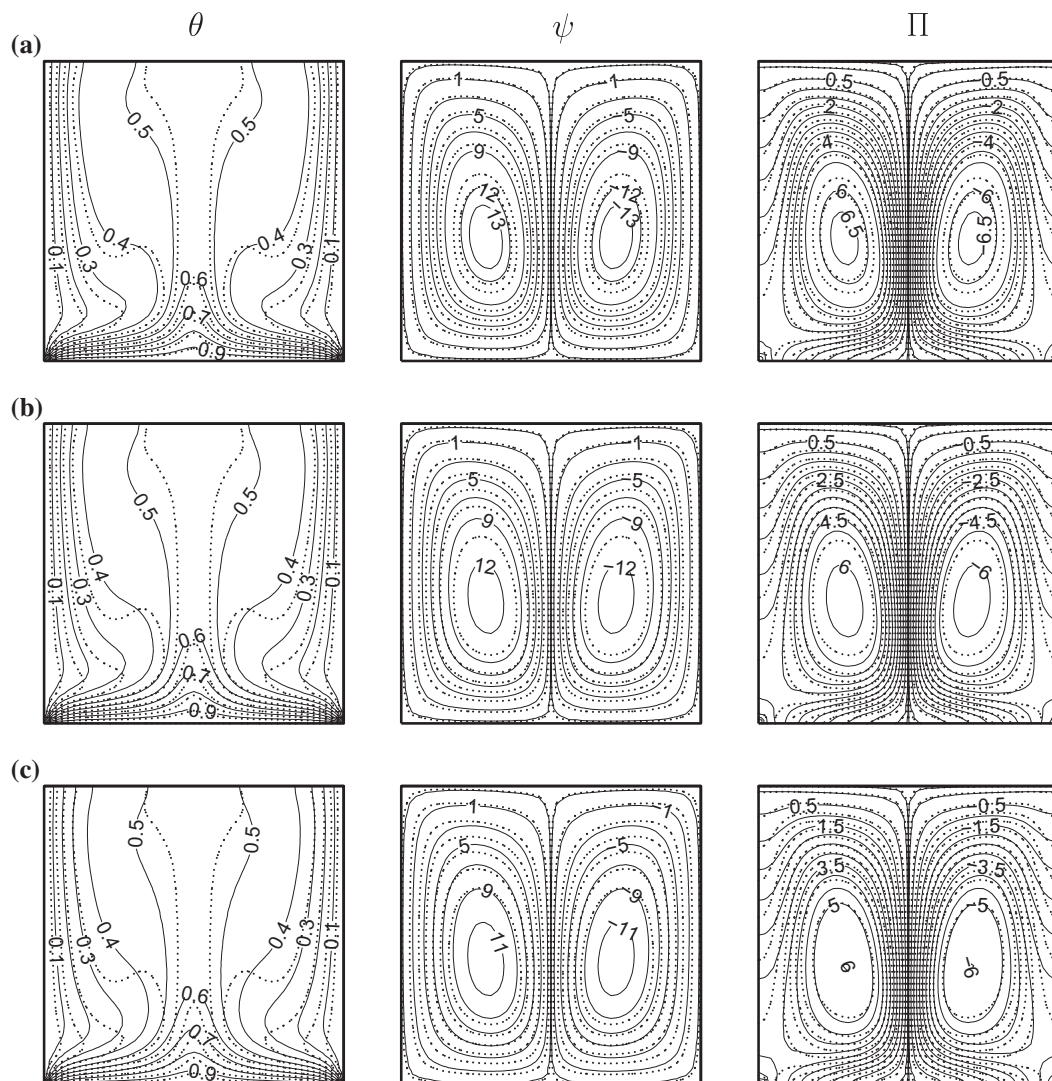


Fig. 7. Temperature (θ), streamfunction (ψ) and heatfunction (II) contours for isothermally hot bottom and cold side walls of TiO_2 –Water nanofluids ($Ra = 10^5$) with (a) $\phi = 0.1$, (b) $\phi = 0.15$ and (c) $\phi = 0.2$, water and –, nanofluid. The labels of contours are shown for solid lines (–) and the contours with dotted line (...) and solid line (–) are shown for specific labels.

other hand, the same regime is relatively cooler with nanofluid for all ϕ s. Similar to previous case with lower Ra as seen in Fig. 5, the heatlines of higher heatfunction values of nanofluids coincide with heatline of lower heatfunctions for water along the walls. The deviations of magnitudes of coinciding heatlines are more along the bottom portion of side walls. Detailed analysis on the correlation between the heatfunctions and Nusselt numbers for various walls will be discussed later.

Fig. 7a–c illustrate temperature, streamfunction and heatfunctions for water and nanofluids (TiO₂–Water) in presence of uniform heating. Results are shown for various solid fractions ($\phi = 0.1, 0.15$ and 0.2) at $Ra = 10^5$. Similar to previous case (Fig. 6), enhanced convection for water is seen at the center of each circulation cell. It is also interesting to note from Table 1 that the density and thermal conductivity of TiO₂ are much smaller than those of Cu. Therefore buoyancy will be even weaker compared to Cu–Water. It is interesting to observe that convection is even much suppressed with TiO₂–Water system. Note that, the central streamline cell for TiO₂–Water corresponds to $|\psi| = 13, 12$ and 11 for $\phi = 0.1, 0.15$ and 0.2 , respectively (Fig. 7a–c) whereas those values for Cu–Water system are $14, 13$ and 13 . Similar to Cu–Water system, a large central region is maintained within $\theta = 0.5 - 0.6$ due to

dominant conductive heat transport. Significant difference in temperature gradient is observed along the side walls for large solid fraction ($\phi = 0.2$) and the isotherm with $\theta = 0.2$ for nanofluid coincides with $\theta = 0.3$ for water (see Fig. 7c). Heatlines illustrate that convective heat transport is greatly reduced due to nanofluids as seen from heatfunction values of the central heatline cell. It is found that $|II| = 6.5$ corresponds to innermost heatline cell for $\phi = 0.1$ and the cell size corresponding to $|II| = 6.5$ is gradually reduced with ϕ . The magnitude of heatfunction of the innermost cell is found to be 6 for $\phi = 0.15$ (Fig. 7b) and finally the tiny central heatline cell corresponds to $|II| = 6$ for $\phi = 0.2$ (Fig. 7c). Similar to previous case with Cu–Water system, the heatlines with smaller magnitudes of water coincide with those with higher magnitudes of TiO₂–Water along the side walls.

Fig. 8a–c display streamlines, isotherms and heatlines for Cu–Water nanofluid with various values of ϕ at $Ra = 10^5$ in presence of sinusoidal heating of bottom wall. Similar to uniform heating case (Fig. 6), the flow strength is found to be stronger for water. Note that, a small flow cell with $|\psi| = 13$ appears for $\phi = 0.1$ whereas the innermost small cell corresponds to $|\psi| = 12$ and 11 for $\phi = 0.2$ and 0.3 , respectively at the center of each vortex. It is interesting to observe that, flow strength of nanofluid with

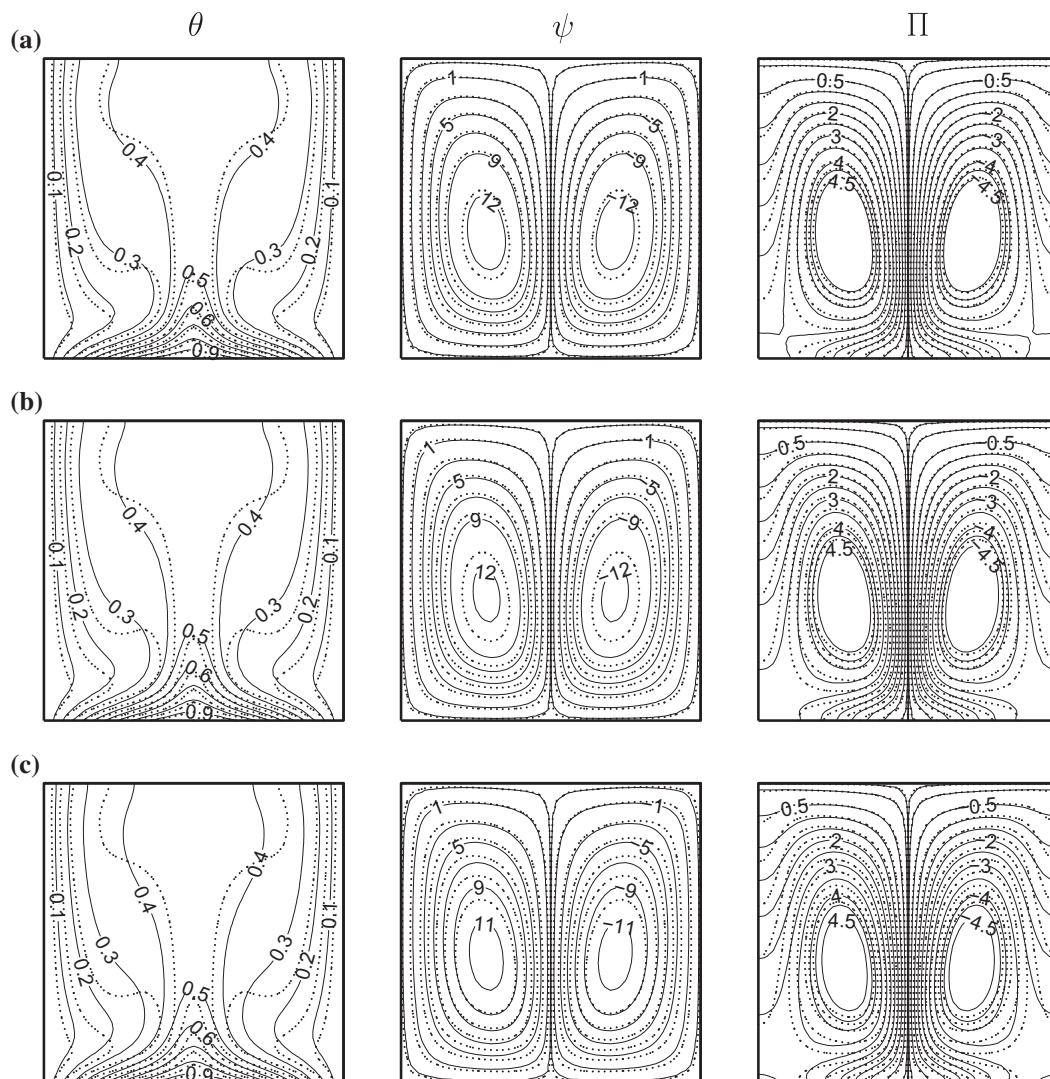


Fig. 8. Temperature (θ), streamfunction (ψ) and heatfunction (II) contours for sinusoidally heated bottom wall and isothermally cold side walls of Cu–Water nanofluids ($Ra = 10^5$) with (a) $\phi = 0.1$, (b) $\phi = 0.15$ and (c) $\phi = 0.2$, water and —, nanofluid. The labels of contours are shown for solid lines (—) and the contours with dotted line (...) and solid line (—) are shown for specific labels.

non-isothermal heating is even weaker than that with isothermal heating. It may be noted that, $|\psi|_{\max} = 14.5, 14$ and 13.24 for $\phi = 0.1, 0.15$ and 0.2 , respectively for uniform heating whereas the corresponding values of $|\psi|_{\max}$ are $13, 12.54$ and 11.88 for non-uniform heating case. Due to overall less heating effect, the top portion of central zone is cooler for non isothermal heating situation compared to isothermal heating situation of the bottom wall (see Figs. 6a–c and 8a–c). Similar to uniform heating situation, the conductive heat transport for nanofluids is dominant near the central zone of the cavity. It is interesting to observe that, due to less intense heating for non-isothermal heating of bottom wall, the dominant conductive effect is not observed for nanofluid near the top portion of the central zone. Therefore, the zone bounded within $\theta = 0.4$ – 0.5 is larger for nanofluid near the bottom portion whereas that zone is larger near the top portion of central zone for water. Similar to uniform heating situation, significant difference in temperature gradients is observed for nanofluids and water near the side wall. Convective heat transport for water is dominant at the center compared to all fractions of nanofluids based on magnitudes of heatlines and similar observations were also made for uniform heating situation. Heatlines also illustrate that heatlines with smaller values of heatfunctions for water coincide with heatlines with higher magnitudes for nanofluids.

Fig. 9a and b illustrate distribution of local Nusselt number vs distance for bottom and left walls, respectively in presence of isothermal bottom heating. Upper panel of the plots represents variation for $Ra = 10^3$ and lower panel corresponds to $Ra = 10^5$. Common to all plots is to note that identical trends on distributions of Nusselt numbers occur for nanofluids and water. However, local

Nusselt numbers (Nu_b and Nu_l) are found to be the largest for $\phi = 0.2$ irrespective of Ra . The enhancement of Nu_b is due to higher thermal conductivity based on Eq. (31) and the parallel distribution curves are further due to the fact that identical distribution of isotherms for water and nanofluids as seen in Fig. 5. Fig. 9a illustrate that the characteristics curves for various ϕ are parallel to each other at $Ra = 10^3$ (upper panel plot). Heatlines also exhibit similar qualitative trends and the larger values of Nu_b are further demonstrated based on the fact that the heatlines of smaller magnitudes of heatfunctions of water coincide with the heatlines of higher magnitudes of nanofluids. Based on Fig. 5, it is found that heatlines are denser near the edges signifying the larger values of Nu_b whereas smaller magnitudes of heatfunction with smaller gradients at the center indicate smaller values of Nu_b . On the other hand, the characteristics curves for Nu_l are found to be parallel along the bottom portion of the side wall and the difference is narrowed down along the top portion (see upper panel of Fig. 9b). The isotherms for nanofluid and water coincide at the bottom portion of side wall (see Fig. 5) irrespective of ϕ s whereas the thermal gradient due to nanofluid is less compared to that due to water at the top portion of side wall. Thus, the enhancement of Nu_l is less for the nanofluid at the top portion of the side wall. Heatlines clearly illustrate that the deviation of magnitudes of heatfunctions for coinciding heatlines is larger along the bottom portion of side wall signifying the enhancement of heat transfer rate at the bottom portion. Common to water and nanofluids, the denser heatlines near the bottom portion of the side wall denote the larger values of Nu_l .

The bottom panel of Fig. 9a illustrates the distributions for Nu_b for various ϕ at $Ra = 10^5$. The edges of the bottom wall correspond

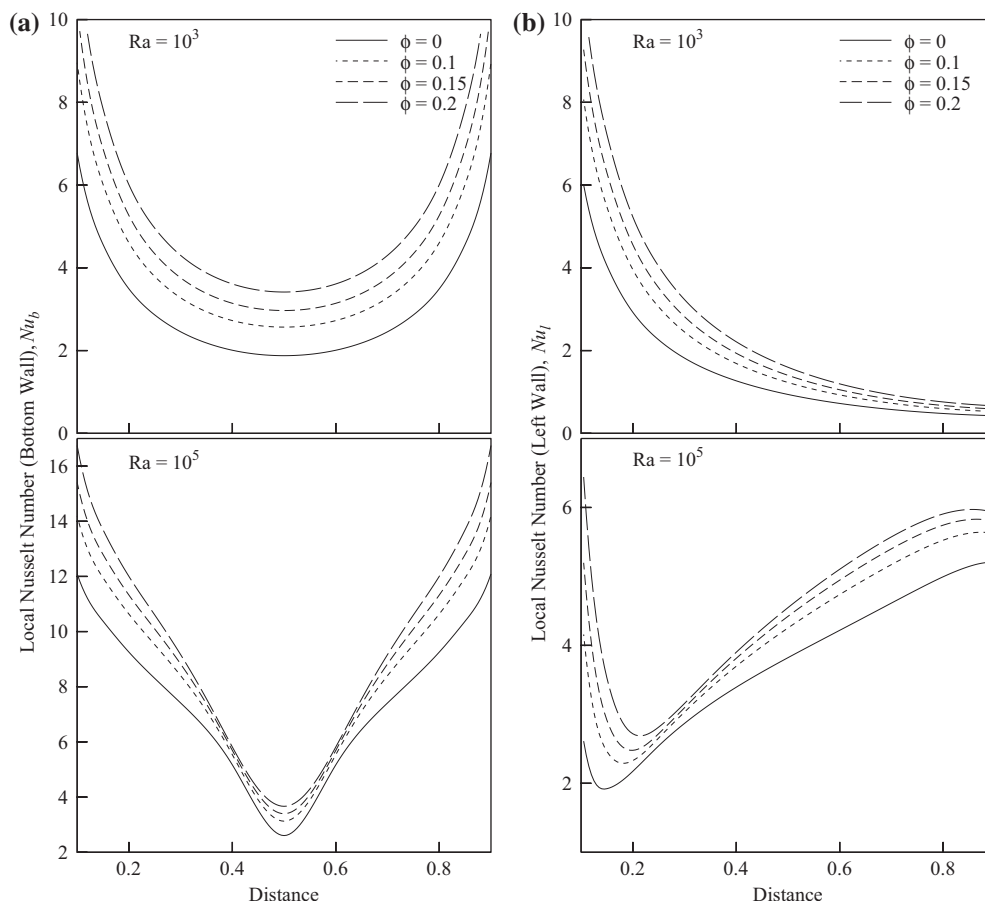


Fig. 9. Local Nusselt numbers [(a) Nu_b and (b) Nu_l] vs distance for various volume fractions (ϕ) of Copper–Water nanofluids in presence of isothermal bottom heating. Upper and lower panels of Figs. (a) and (b) represent $Ra = 10^3$ and 10^5 , respectively.

to large heat transfer rates both for nanofluids and water due to singularity of temperature boundary conditions. Heat transfer rates are even larger for nanofluids with $\phi = 0.2$. The deviations of values of heatfunctions for coinciding heatlines are larger near the edges compared to those near the center of the bottom wall as seen in Fig. 6. Consequently, the enhancement of heat transfer rates is more near the edges. Similar to situation with $Ra = 10^3$, Nu_b is less at the center based on least gradient of heatfunctions (Π).

Interesting trend on Nu_l is observed for $Ra = 10^5$ (see lower panel of Fig. 9b). It is found that Nu_l is largest at the bottom edge of the side wall, that decreases till a distance near to the bottom edge and further, Nu_l increases monotonically till the top of the wall. Nanofluids exhibit larger heat transfer rates along the entire distance and the rates increase with ϕ at a particular distance. Common to nanofluid and water, the thermal boundary layer thickness is found to increase till a zone near the edge and thus, Nu_l attains a minimum value. The thermal boundary layer thickness is smaller near the top portion of the side wall and thus Nu_l attains a maxima.

Heatlines illustrate that highly concentrated heatlines connect the left and bottom walls near the edges due to conduction dominant heat transfer. Therefore, Nu_l shows maxima at that zone. Highly disperse heatlines are observed near the zone corresponding to large thickness of thermal boundary layer which also corresponds to smaller values of Nu_l . Further dense heatlines are observed near the top portion of side walls indicating larger values of Nu_b . Similar to previous cases, the heatlines of smaller values of heatfunctions for water coincide with those of smaller values of

heatfunctions of nanofluids. Thus, Nu_l is largest for $\phi = 0.2$ at any location.

Fig. 10a and b show distributions of local Nusselt number vs distance for bottom and left walls, respectively in presence of sinusoidally heated bottom wall. Upper panel corresponds to $Ra = 10^3$ and lower panel represents distributions for $Ra = 10^5$. Identical qualitative trends in Nusselt numbers are found for nanofluids and water. Similar to previous case with isothermal bottom heating wall, local Nusselt numbers (Nu_l and Nu_b) are found to be largest irrespective of distance and Ra for $\phi = 0.2$. The enhancement of Nusselt numbers is due to higher thermal conductivity based on Eq. (30). Fig. 10a illustrates that the distributions of Nu_b are parallel to each other for all ϕ s at $Ra = 10^3$. This is due to the fact that isotherms and flow characteristics show identical qualitative distributions at $Ra = 10^3$ (Figures not shown). Similar trends were also observed for isothermal heating of bottom wall (see Fig. 9a). Heatlines further demonstrate the dense heatlines near the center of the bottom wall and they are dispersed along the edges of the bottom wall (Figure not shown). Therefore, Nu_b is largest at the center of the bottom wall. Similar to isothermal bottom heating situation, the distributions for Nu_l are parallel and the differences are narrowed down at the top of the side walls (upper panel of Fig. 10b). The denser heatlines were found near the bottom portion of side walls and Nu_l is found to be maximum at the bottom.

The bottom panel of Fig. 10a illustrates the distributions for Nu_b with various ϕ at $Ra = 10^5$. The local heat transfer rates follow sinusoidal distribution. The maxima occur at intermediate locations, $X = 0.3$ and 0.7 and the minima are found at center and edges of the bottom wall. Although the enhancement of heat

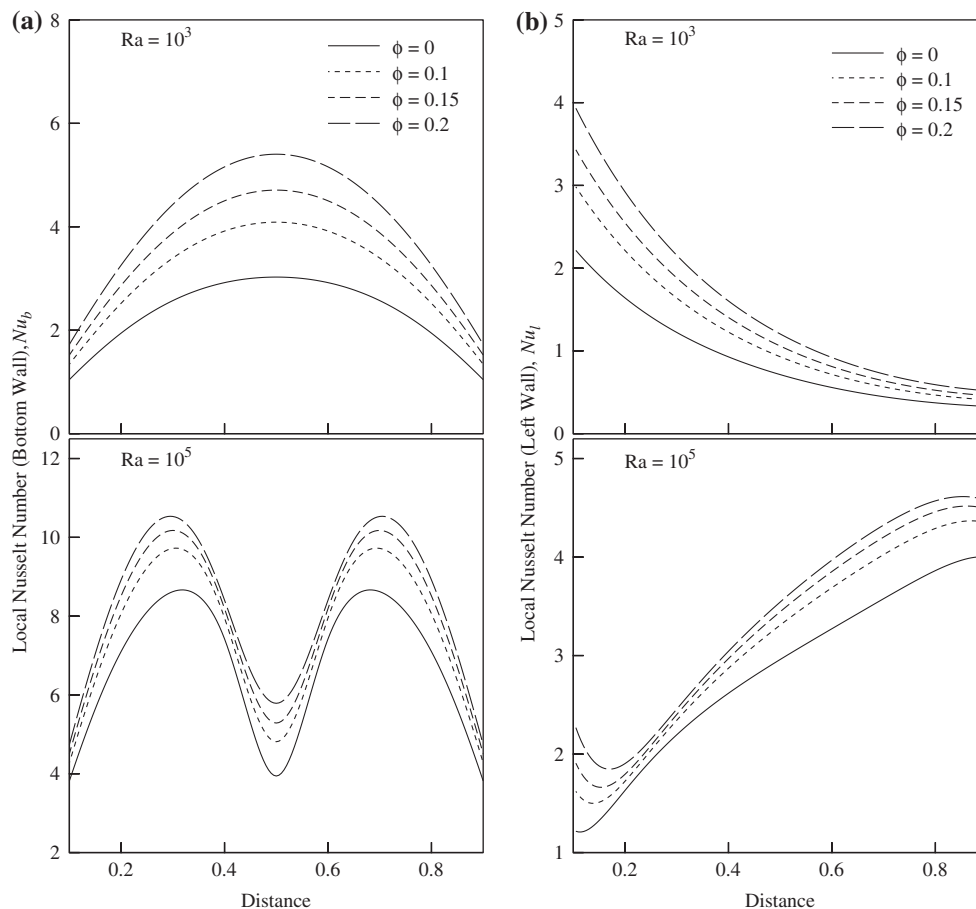


Fig. 10. Local Nusselt numbers [(a) Nu_b and (b) Nu_l] vs distance for various volume fractions (ϕ) of Copper–Water nanofluids in presence of sinusoidal bottom heating. Upper and lower panels of Figs. (a) and (b) represent $Ra = 10^3$ and 10^5 , respectively.

transfer rates are found for higher ϕ s at all distances, but the largest increase in rates are found at $X = 0.3$ and 0.7 . As explained earlier, the deviations of values of heatfunctions for coinciding heatlines are maximum at these locations (see Fig. 8c). It is interesting to observe that the heatlines are highly disperse near the corners of the bottom wall. Consequently, the heat transfer rates are less at the corners and the enhancement of heat transfer rates is also found to be least compared to other locations. The heat transfer rates are also found to be smaller at the central zone of the bottom wall due to the heatlines with smaller heatfunction values. Similar situation was also found in earlier case as seen the bottom panel of Fig. 9a.

The local heat transfer rates at the left wall (Nu_l) for $Ra = 10^3$ and $Ra = 10^5$ are displayed in top and bottom panels of Fig. 10b, respectively. The qualitative trends of Nu_l for isothermal and sinusoidal heating walls for both Ra values are same. However, the heat transfer rates at the bottom portion of the side wall are quite less due to highly disperse heatlines compared to case 1 with uniform heating of bottom wall. Degree of enhancement of heat transfer rates is almost similar order of magnitudes near the top portion of the side walls.

Fig. 11a and b display comparative analysis on average Nusselt numbers of the bottom wall (\overline{Nu}_b) for water, Cu–Water, TiO_2 –Water and Alumina–Water nanofluids at a few representative values of Ra . Common to all situations, there is a significant enhancement of \overline{Nu}_b at all Ra values for $\phi = 0.1$ and 0.2 . Upper panel plots show the variations for $\phi = 0.1$ and lower panel plots correspond to $\phi = 0.2$. It is interesting to observe that the variations of average Nusselt numbers (\overline{Nu}_b) are within similar ranges for

$Ra = 10^3$ and 10^4 with both $\phi = 0.1$ and 0.2 . The average Nusselt number may be slightly larger for $Ra = 10^4$ with specific cases and the similar order of magnitudes of \overline{Nu}_b are due to smaller degree of enhancement of heat transfer due to dominant viscous force for various values of ϕ . In contrast, the average Nusselt numbers for nanofluids (specially Copper–Water and Alumina–Water) show dramatic enhancement at $Ra = 10^5$ for both $\phi = 0.1$ and 0.2 due to enhanced buoyancy force at $Ra = 10^5$. In general, the enhancement of heat transfer rates are smaller for non-isothermal heating of bottom wall situations as seen in Fig. 11a and b.

3.4. Conclusion

Finite element based simulations on flow and thermal characteristics are performed to illustrate the enhancement of heat transfer rates for various nanofluids (Copper–Water, Alumina–Water and TiO_2 –Water) in presence of various thermal boundary conditions. Enhancement of heat transfer rates has been illustrated via isotherms associated with trajectory of heat flow via heatline method. Two types of boundary conditions are considered: hot left and cold right walls in presence of adiabatic horizontal walls (case 1) and hot bottom wall with cold side walls in presence of adiabatic top wall (case 2). Influence of nanoparticles on flow and thermal characteristics for cases 1 and 2 have been outlined below.

- Unicellular streamlines and heatlines are observed for case 1 type boundary conditions whereas two oppositely rotated circulation patterns are observed for case 2.

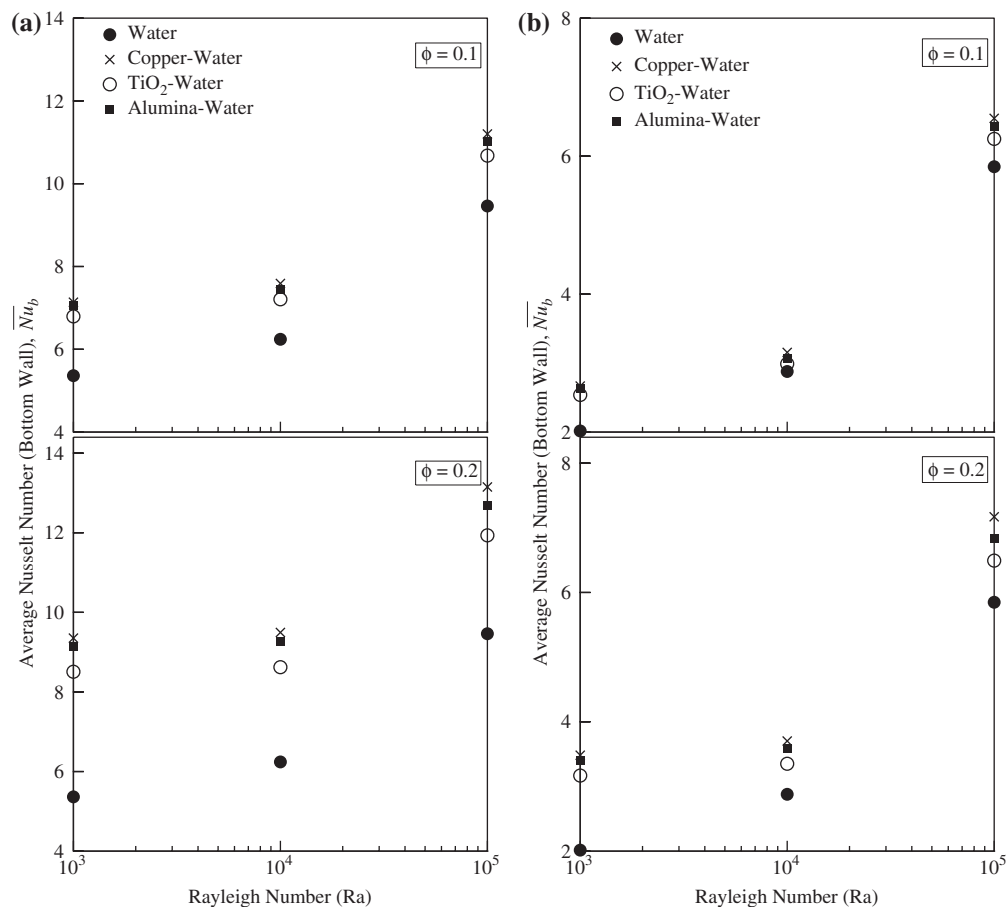


Fig. 11. Average Nusselt number (\overline{Nu}_b) vs Rayleigh numbers of water and nanofluids (Copper–Water, TiO_2 –Water and Alumina–Water) for (a) isothermal bottom heating and (b) sinusoidal bottom heating situations. Upper and lower panels of Figs. (a) and (b) represent $\phi = 0.1$ and 0.2 , respectively.

- It is observed that flow strength as well as convective heat flow are dominant for water at the center of the cavity especially for $Ra \leq 10^4$ due to dominance of viscous force. For unicellular flow patterns, the convective heat transport is dominant at the core for water whereas the conductive heat transfer is dominant for nanofluids especially at $Ra = 10^3$. Similar to case 1, the core of each circulation cell has smaller flow strength of nanofluids compared to that of water for case 2. Heatlines demonstrate that the convective heat flow patterns with closed loop heatlines are observed for water whereas the closed loop heatlines are completely absent for nanofluids especially for case 1 at $Ra \leq 10^3$.
- Convective heat transport is found to be dominant for nanofluids. Comparative studies with water depict that the streamlines with larger magnitudes of streamfunctions for nanofluids coincide with streamlines with lesser values of streamfunctions for water at $Ra = 10^5$. Similar features are also observed for heatlines and heatfunctions for closed loop heatlines at the core of a circulation cell.
- Local Nusselt numbers for nanofluids show larger values compared to that of water for all values of Ra . This trend is further confirmed by the fact that heatlines of larger heatfunctions for nanofluids coincide with heatlines of smaller magnitude of water along the bottom and side walls for both the cases (case 1 and 2) in the entire range of Ra .
- Overall enhancement of heat transfer rates are further demonstrated via average Nusselt numbers. It is interesting to observe that the enhancement of heat transfer rates due to nanofluids are of similar order of magnitudes for $Ra \leq 10^4$ exhibiting the dominance of viscous force due to nanofluids. In contrast, the heat transport rate due to nanofluids dramatically enhance for $Ra = 10^5$ due to dominance of buoyancy force for nanofluids. The dramatic enhancement of heat transfer rates for nanofluids is also found to correspond largely dense heatlines.
- It is observed that Copper–Water and Alumina–Water exhibit larger enhancement of heat transfer.
- Case 2 type of boundary conditions also show larger heat transfer rates for all nanofluids.

Acknowledgment

Authors would like to thank anonymous reviewer for critical comments and suggestions which improved the quality of the manuscript.

References

- [1] S.U.S. Choi, Enhancing thermal conductivity of fluids with nanoparticles, developments and applications of non-Newtonian flows, in: D.A. Siginer, H.P. Wang (Eds.), *The American Society of Mechanical Engineers*, New York, FED – vol. 231/MD – vol. 66, pp. 99–103.
- [2] J.A. Eastman, S.U.S. Choi, S. Li, L.J. Thompson, S. Lee, Enhanced thermal conductivity through the development of nanofluids, in: S. Komarneni, J.C. Parker, H.J. Wollenberger (Eds.), *Nanophase and Nanocomposite Materials II*, MRS, Pittsburgh, PA, 1997, pp. 3–11.
- [3] J.A. Eastman, S.U.S. Choi, S. Li, W. Yu, L.J. Thompson, Anomalous increased effective thermal conductivities of ethylene glycol-based nano-fluids containing copper nano-particles, *Appl. Phys. Lett.* 78 (2001) 718–720.
- [4] S.U.S. Choi, Z.G. Zhang, W. Yu, F.E. Lockwood, E.A. Grulke, Anomalous thermal conductivity enhancement in nano-tube suspensions, *Appl. Phys. Lett.* 79 (2001) 2252–2254.
- [5] S.K. Das, N. Putra, P. Thiesen, W. Roetzel, Temperature dependence of thermal conductivity enhancement for nanofluids, *ASME J. Heat Transfer* 125 (2003) 567–574.
- [6] P. Keblinski, S.R. Phillpot, S.U.S. Choi, J.A. Eastman, Mechanisms of heat flow in suspensions of nano-sized particles (nanofluids), *Int. J. Heat Mass Transfer* 45 (4) (2002) 855–863.
- [7] B.X. Wang, H. Li, X.F. Peng, Research on the heat conduction enhancement for liquid with nanoparticles suspensions, General Paper (G-1), in: *Int. Symp. Therm. Sci. Eng.* (TSE 2002), 23–26 October, Beijing, 2002.
- [8] B.X. Wang, L.P. Zhou, X.F. Peng, A fractal model for predicting the effective thermal conductivity of liquid with suspension of nanoparticles, *Int. J. Heat Mass Transfer* 46 (2003) 2665–2672.
- [9] R.L. Hamilton, O.K. Crosser, Thermal conductivity of heterogeneous two component systems, *I & EC Fundam.* 1 (1962) 187–191.
- [10] F.J. Wasp, *Solid–Liquid Flow Slurry Pipeline Transportation*, Trans. Tech. Publ., Berlin, 1977.
- [11] J.C. Maxwell–Garnett, Colours in metal glasses and in metallic films, *Philos. Trans. Roy. Soc. A* 203 (1904) 385–420.
- [12] D.A.G. Bruggeman, Berechnung verschiedener physikalischer konstanten von heterogenen substanzen, I. Dielektrizitätskonstanten und Leitfähigkeiten der Mischkörper aus Isotropen Substanzen, *Ann. Physik. Leipzig* 24 (1935) 636–679.
- [13] W. Yu, S.U.S. Choi, The role of interfacial layers in the enhanced thermal conductivity of nanofluids: a renovated Maxwell model, *J. Nanopart. Res.* 5 (2003) 167–171.
- [14] S. Kumar, S.K. Prasad, J. Banerjee, Analysis of flow and thermal field in nanofluid using a single phase thermal dispersion model, *Appl. Math. Model.* 34 (3) (2010) 573–592.
- [15] K. Khanafer, K. Vafai, M. Lightstone, Buoyancy driven heat transfer enhancement in a two-dimensional enclosure utilizing nanofluids, *Int. J. Heat Mass Transfer* 46 (2003) 3639–3653.
- [16] S.P. Jang, S.U.S. Choi, Free convection in a rectangular cavity (Benard convection) with nanofluids, *Proceedings of the IMECE*, Anaheim, California, USA, 2004.
- [17] R.Y. Jou, S.C. Tzeng, Numerical research of nature convective heat transfer enhancement filled with nanofluids in rectangular enclosures, *Int. Commun. Heat Mass Transfer* 33 (2006) 727–736.
- [18] K.S. Hwang, J.H. Lee, S.P. Jang, Buoyancy-driven heat transfer of water-based Al_2O_3 nanofluids in a rectangular cavity, *Int. J. Heat Mass Transfer* 50 (2007) 4003–4010.
- [19] X.-Q. Wang, A.S. Mujumdar, C. Yap, Free convection heat transfer in horizontal and vertical rectangular cavities filled with nanofluids, in: *International Heat Transfer Conference IHTC-13*, Sydney, Australia, 2006.
- [20] G.A. Sheikhzadeh, A. Arefmanesh, M. Mahmoodi, Numerical study of natural convection in a differentially-heated rectangular cavity filled with TiO_2 –water nanofluid, *J. Nano Res.* 13 (2011) 75–80.
- [21] Z. Alloui, P. Vasseur, M. Reggio, Natural convection of nanofluids in a shallow cavity heated from below, *Int. J. Therm. Sci.* 50 (3) (2011) 385–393.
- [22] A.K. Santra, S. Sen, N. Chakraborty, Study of heat transfer augmentation in a differentially heated square cavity using copper–water nanofluid, *Int. J. Therm. Sci.* 47 (2008) 1113–1122.
- [23] C.J. Ho, M.W. Chen, Z.W. Li, Numerical simulation of natural convection of nanofluid in a square enclosure: effects due to uncertainties of viscosity and thermal conductivity, *Int. J. Heat Mass Transfer* 51 (17–18) (2008) 4506–4516.
- [24] H.F. Oztop, E. Abu-Nada, Numerical study of natural convection in partially heated rectangular enclosures filled with nanofluids, *Int. J. Heat Fluid Flow* 29 (2008) 1326–1336.
- [25] E. Abu-Nada, Application of nanofluids for heat transfer enhancement of separated flows encountered in a backward facing step, *Int. J. Heat Fluid Flow* 29 (2008) 242–249.
- [26] E. Abu-Nada, Effects of variable viscosity and thermal conductivity of Al_2O_3 –Water nanofluid on heat transfer enhancement in natural convection, *Int. J. Heat Fluid Flow* 30 (2009) 679–690.
- [27] S.M. Aminossadati, B. Ghasemi, Natural convection cooling of a localised heat source at the bottom of a nanofluid-filled enclosure, *Eur. J. Mech. B/Fluids* 28 (2009) 630–640.
- [28] E. Abu-Nada, H.F. Oztop, Effects of inclination angle on natural convection in enclosures filled with Cu–Water nanofluid, *Int. J. Heat Fluid Flow* 30 (4) (2009) 669–678.
- [29] B. Ghasemi, S.M. Aminossadati, Periodic natural convection in a nanofluid-filled enclosure with oscillating heat flux, *Int. J. Therm. Sci.* 49 (2010) 1–9.
- [30] H.F. Oztop, E. Abu-Nada, Y. Varol, K. Al-Salem, Computational analysis of non-isothermal temperature distribution on natural convection in nanofluid filled enclosures, *Superlattices and Microstruct.* 49 (4) (2011) 453–467.
- [31] E.B. Ogut, Natural convection of water-based nanofluids in an inclined enclosure with a heat source, *Int. J. Therm. Sci.* 48 (2009) 2063–2073.
- [32] C.J. Ho, W.K. Liu, Y.S. Chang, C.C. Lin, Natural convection heat transfer of alumina–water nanofluid in vertical square enclosures: an experimental study, *Int. J. Therm. Sci.* 49 (8) (2010) 1345–1353.
- [33] S.M. Aminossadati, B. Ghasemi, Natural convection of water–CuO nanofluid in a cavity with two pairs of heat source–sink, *Int. Commun. Heat Mass Transfer* 38 (5) (2011) 672–678.
- [34] D.A. Nield, A.V. Kuznetsov, The effect of vertical throughflow on thermal instability in a porous medium layer saturated by a nanofluid, *Transport Porous Media* 87 (3) (2011) 765–775.
- [35] N.M. Arifin, R. Nazar, I. Pop, Non-isobaric Marangoni boundary layer flow for Cu, Al_2O_3 and TiO_2 nanoparticles in a water based fluid, *Meccanica* 46 (4) (2011) 833–843.
- [36] B. Ghasemi, S.M. Aminossadati, A. Raisi, Magnetic field effect on natural convection in a nanofluid-filled square enclosure, *Int. J. Therm. Sci.* 50 (9) (2011) 1748–1756.
- [37] S. Kimura, A. Bejan, The heatline visualization of convective heat transfer, *J. Heat Transfer* 105 (1983) 916–919.
- [38] A. Bejan, *Convection Heat Transfer*, third ed., Wiley, New York, 2004.

- [39] F.L. Bello-Ochende, A heat function formulation for thermal convection in a square cavity, *Int. Commun. Heat Mass Transfer* 15 (1988) 193–202.
- [40] A.M. Morega, A. Bejan, Heatline visualization of forced-convection laminar boundary layers, *Int. J. Heat Mass Transfer* 36 (1993) 3957–3966.
- [41] F.Y. Zhao, D. Liu, G.F. Tang, Application issues of the streamline, heatline and massline for conjugate heat and mass Transfer, *Int. J. Heat Mass Transfer* 50 (2007) 320–334.
- [42] V.A.F. Costa, Unification of the streamline, heatline and massline methods for the visualization of two-dimensional transport phenomena, *Int. J. Heat and Mass Transfer* 42 (1999) 27–33.
- [43] V.A.F. Costa, Bejan's heatlines and masslines for convection visualization and analysis, *Appl. Mech. Rev.* 59 (2006) 126–145.
- [44] S.K. Dash, Heatline visualization in turbulent flow, *Int. J. Numer. Methods Heat Fluid Flow* 6 (1996) 37–46.
- [45] F.Y. Zhao, D. Liu, G.F. Tang, Natural convection in an enclosure with localized heating and salting from below, *Int. J. Heat Mass Transfer* 51 (2008) 2889–2904.
- [46] A.M. Morega, A. Bejan, Heatline visualization of forced convection in porous media, *Int. J. Heat Fluid Flow* 15 (1994) 42–47.
- [47] F.Y. Zhao, D. Liu, G.F. Tang, Natural convection in a porous enclosure with a partial heating and salting element, *Int. J. Therm. Sci.* 47 (2008) 569–583.
- [48] D. Liu, F.Y. Zhao, H.Q. Wang, Passive heat and moisture removal from a natural vented enclosure with a massive wall, *Energy* 36 (5) (2011) 2867–2882.
- [49] F.Y. Zhao, D. Liu, G.F. Tang, Determining boundary heat flux profiles in an enclosure containing solid conducting block, *Int. J. Heat Mass Transfer* 53 (7–8) (2010) 1269–1282.
- [50] T. Basak, S. Roy, A.R. Balakrishnan, Effects of thermal boundary conditions on natural convection flows within a square cavity, *Int. J. Heat Mass Transfer* 49 (2006) 4525–4535.
- [51] J.C. Maxwell, *A Treatise on Electricity and Magnetism*, third ed., Oxford University Press, Cambridge, UK, 1891.
- [52] H.C. Brinkman, The viscosity of concentrated suspensions and solution, *J. Chem. Phys.* 20 (1952) 571–581.
- [53] J.N. Reddy, *An Introduction to the Finite Element Method*, McGraw-Hill, New York, 1993.
- [54] T. Basak, S. Roy, Role of 'Bejan's heatlines' in heat flow visualization and optimal thermal mixing for differentially heated square enclosures, *Int. J. Heat Mass Transfer* 51 (2008) 3486–3503.
- [55] G.K. Batchelor, *An Introduction to Fluid Dynamics*, Cambridge University Press, 1993.
- [56] G.D. Vahl Davis, Natural convection of air in a square cavity, a bench mark numerical solution, *Int. J. Numer. Methods Fluid* 3 (1983) 249–264.
- [57] N.C. Markatos, K.A. Pericleous, Laminar and turbulent natural-convection in an enclosed cavity, *Int. J. Heat Mass Transfer* 27 (5) (1984) 755–772.
- [58] G.V. Hadjisophocleous, A.C.M. Sousa, J.E.S. Venart, Prediction of transient natural-convection in enclosures of arbitrary geometry using a nonorthogonal numerical-model, *Numer. Heat Transfer* 13 (3) (1988) 373–392.